

# Systematic search for singularities in 3D Euler flows

Xinyu Zhao<sup>1</sup> and Bartosz Protas<sup>1,\*</sup>

<sup>1</sup>Department of Mathematics and Statistics, McMaster University  
Hamilton, ON, Canada

February 20, 2024

## Abstract

We consider the question whether starting from a smooth initial condition 3D inviscid Euler flows on a periodic domain may develop singularities in a finite time. Our point of departure is the well-known result by Kato (1972), which asserts the local existence of classical solutions to the Euler system in the Sobolev space  $H^m$  for  $m > 5/2$ . Thus, the potential formation of a singularity must be accompanied by an unbounded growth of the  $H^m$  norm of the velocity field as the singularity time is approached. We perform a systematic search for “extreme” Euler flows that may realize such a scenario by formulating and solving a PDE-constrained optimization problem where the  $H^3$  norm of the solution at a certain fixed time  $T > 0$  is maximized with respect to the initial data subject to suitable normalization constraints. This problem is solved using a state-of-the-art Riemannian conjugate gradient method where the gradient is obtained from solutions of an adjoint system. Computations performed with increasing numerical resolutions demonstrate that, as asserted by the theorem of Kato (1972), when the optimization time window  $[0, T]$  is sufficiently short, the  $H^3$  norm remains bounded in the extreme flows found by solving the optimization problem, which indicates that the Euler system is well-posed on this “short” time interval. On the other hand, when the window  $[0, T]$  is long, possibly longer than the time of the local existence asserted by Kato’s theorem, then the  $H^3$  norm of the extreme flows diverges upon resolution refinement, which indicates a possible singularity formulation on this “long” time interval. The extreme flow obtained on the long time window has the form of two colliding vortex rings and is characterized by certain symmetries. In particular, the region of the flow in which a singularity might occur is nearly axisymmetric.

## 1 Introduction

The motion of an ideal (inviscid) incompressible fluid on a domain  $\Omega \subseteq \mathbb{R}^3$  is described by the Euler equations

$$\begin{aligned} \frac{\partial \mathbf{u}}{\partial t} + (\mathbf{u} \cdot \nabla) \mathbf{u} &= -\nabla p, & (\mathbf{x}, t) \in \Omega \times (0, T], \\ \nabla \cdot \mathbf{u} &= 0, & (\mathbf{x}, t) \in \Omega \times (0, T], \\ \mathbf{u}|_{t=0} &= \boldsymbol{\eta}, & \mathbf{x} \in \Omega, \end{aligned} \tag{1.1}$$

where  $\nabla = [\partial_1, \partial_2, \partial_3]^T$  is the gradient operator,  $\mathbf{u} = \mathbf{u}(\mathbf{x}, t) = [u_1, u_2, u_3]^T$  is the velocity field,  $p = p(\mathbf{x}, t)$  is the scalar pressure and  $T > 0$  is the length of the time window considered. We assume the flow domain to be a periodic unit cube  $\Omega = \mathbb{T}^3 := \mathbb{R}^3/\mathbb{Z}^3$ , where “:=” means “equal to by definition”. In system (1.1), the symbol  $\boldsymbol{\eta}$  denotes the initial condition for the velocity which is assumed to satisfy  $\nabla \cdot \boldsymbol{\eta} = 0$ . We will use the notation  $\mathbf{u}(t; \boldsymbol{\eta})$  to indicate the dependence of the solution of system (1.1) at time  $t$  on  $\boldsymbol{\eta}$ . We are interested in the possibility

---

\*Corresponding Author, Email: bprotas@mcmaster.ca

of a spontaneous formation of finite-time singularities in solutions of the Euler system (1.1) equipped with smooth initial data, the so-called “blow-up problem”. It remains one of the central open questions in mathematical fluid mechanics (Gibbon et al., 2008) and is closely related to the corresponding regularity problem for the viscous Navier-Stokes system (Doering, 2009; Robinson, 2020), which has been recognized by the Clay Mathematics Institute as one of its “millennium problems” (Fefferman, 2000). Our goal in this paper is to undertake a systematic search for possible singularities in the Euler system (1.1) using methods of numerical PDE optimization.

The first results asserting local existence of classical solutions to the Euler system were obtained by Lichtenstein (1925) for Hölder-regular initial data  $\boldsymbol{\eta} \in C^{1,\alpha}(\mathbb{R}^3)$  with  $0 < \alpha < 1$ . The local existence of classical solutions in Sobolev spaces was then established by Kato (1972) and is summarized in the following theorem

**Theorem 1.1** *If  $\boldsymbol{\eta} \in H^m(\mathbb{T}^3)$  for some  $m > 5/2$  and satisfies  $\nabla \cdot \boldsymbol{\eta} = 0$ , then there exists a time  $T = T(\|\boldsymbol{\eta}\|_{H^m}) > 0$  such that (1.1) has a unique solution  $\mathbf{u}(\cdot; \boldsymbol{\eta}) \in C([0, T]; H^m) \cap C^1([0, T]; H^{m-1})$ .*

The study of the local well-posedness of the Euler system (1.1) with analytic initial data began with the work of Bardos and Benachour (1977).

Another well-known conditional regularity result is the Beale-Kato-Majda (BKM) criterion (Beale et al., 1984; Chen and Pavlović, 2012) which states that a smooth solution  $\mathbf{u}$  of the Euler system develops a singularity at  $t = T^*$  if and only if

$$\lim_{t \rightarrow T^*} \int_0^t \|\boldsymbol{\omega}(\tau)\|_{L^\infty} d\tau = \infty, \quad (1.2)$$

where  $\boldsymbol{\omega} := \nabla \times \mathbf{u}$  is the vorticity field of the flow. The sufficiency of this condition can be deduced from Theorem 1.1 using a Sobolev inequality (Adams and Fournier, 2005)

$$\int_0^t \|\boldsymbol{\omega}(\tau)\|_{L^\infty} d\tau \leq t \sup_{0 \leq \tau \leq t} \|\nabla \mathbf{u}(\tau)\|_{L^\infty} \leq Ct \sup_{0 \leq \tau \leq t} \|\mathbf{u}(\tau)\|_{H^m}, \quad m > 5/2, \quad (1.3)$$

whereas its necessity is a result of the inequality (Majda and Bertozzi, 2002)

$$\|\mathbf{u}(t)\|_{H^m} \leq \|\boldsymbol{\eta}\|_{H^m} \exp \left\{ C_1 \exp \left( C_2 \int_0^t \|\boldsymbol{\omega}(\tau)\|_{L^\infty} d\tau \right) \right\}. \quad (1.4)$$

The double exponential on the right hand side (RHS) of (1.4) suggests that, should blow-up indeed occur at some  $t = T^*$ , we can expect a much more rapid growth of  $\|\mathbf{u}(t)\|_{H^m}$ ,  $m > 5/2$ , than that of  $\|\boldsymbol{\omega}(t)\|_{L^\infty}$ , as  $t \rightarrow T^*$ . There have been various refinements of the BKM criterion, where the  $L^\infty$  norm of vorticity in (1.2) is replaced with a norm in the BMO space (Kozono and Taniuchi, 2000) or a Besov space (Chae, 2001). In addition, there are also geometric criteria for blow-up (Constantin et al., 1996; Deng et al., 2005), in which the direction of the vorticity  $\boldsymbol{\omega}/|\boldsymbol{\omega}|$  plays a crucial role. As was shown in Gibbon (2013), the relative ordering of suitably rescaled vorticity moments provides information about the degree of depletion of the nonlinearity, and hence also about the regularity of solutions. On the other hand, the regularity of weak solutions of the Euler system is related to Onsager’s conjecture concerning energy dissipation in such flows (Constantin et al., 1994) and significant progress has been

made recently as regards the non-uniqueness of weak solutions with low regularity (De Lellis and Székelyhidi Jr, 2019).

With respect to blow-up scenarios, Elgindi (2021) proved that there exist swirl-free axisymmetric solutions of the Euler system corresponding to initial data in  $C^{1,\alpha}(\mathbb{R}^3)$  that can develop finite-time singularities. Elgindi and Jeong (2019) showed the existence of finite-time singularities in strong solutions to axisymmetric Euler equations on exterior domains with “hourglass”-shaped boundaries. Most recently, Chen and Hou (2022) proved a nearly self-similar blow-up of solutions to the 3D axisymmetric Euler equations with smooth initial data on cylindrical domains with solid boundaries. We emphasize that in the last two cases the presence of the solid boundary is key to the formation of the singularity.

The computational studies exploring the possibility of finite-time blow-up in the Euler system include Brachet et al. (1983); Pumir and Siggia (1990); Brachet (1991); Kerr (1993); Pelz (2001); Bustamante and Kerr (2008); Ohkitani and Constantin (2008); Ohkitani (2008); Grafke et al. (2008); Gibbon et al. (2008); Hou (2009); Orlandi et al. (2012); Bustamante and Brachet (2012); Kerr (2013); Orlandi et al. (2014); Campolina and Mailybaev (2018); Larios et al. (2018), all of which considered problems subject to periodic boundary conditions in all three spatial directions. We also mention the studies by Matsumoto et al. (2008) and Siegel and Caffisch (2009), along with references found therein, in which various complexified forms of the Euler equations were investigated. The idea of this approach is that, since solutions to complexified equations have singularities in the complex plane, singularity formation in the real-valued problem is manifested by the collapse of the complex-plane singularities onto the real axis. Some of the investigations (Bustamante and Brachet, 2012; Orlandi et al., 2012) hinted at the possibility of singularity formation in a finite time. In this connection we also highlight the computational investigations of Luo and Hou (2014a,b) in which blow-up was documented in axisymmetric Euler flows on a bounded cylindrical domain. This mechanism of singularity formation involves an interaction with the solid boundary and was recently validated with rigorous mathematical analysis by Chen and Hou (2022). We also mention an investigation by Hou (2022) who provided evidence for blow-up in axisymmetric Euler flows on bounded domains in which singularity occurs away from the boundaries. In contrast to most other studies, the works of Luo and Hou (2014a,b); Hou (2022) relied on adaptive mesh refinement employed to resolve fine structures in flows at the edge of regularity. In this context, we also mention the investigation by Yin et al. (2021) where the Euler system (1.1) was solved in the Lagrangian setting using the characteristic mapping method. Regarding weak solutions and Onsager’s related conjecture, Fehn et al. (2022) recently presented numerical evidence for nonvanishing energy dissipation in weak solutions of the Euler system (1.1) which was obtained using a method based on a discontinuous Galerkin approximation.

While in the aforementioned computational studies the initial conditions for the Euler system were chosen in an ad-hoc manner, albeit one usually motivated by deep physical considerations, here we follow a fundamentally different approach wherein the initial condition leading to the most singular, in a mathematically precise sense, solutions is sought systematically by solving a suitably constrained PDE optimization problem. This approach was originally proposed by Lu and Doering (2008) as a way to determine incompressible velocity fields maximizing the instantaneous growth rate of enstrophy in 3D Navier-Stokes flows. It was later extended by Ayala and Protas (2011, 2014, 2017), Yun and Protas (2018) to study extreme behavior in solutions of different hydrodynamic models such as variants of the Burgers

equation. Recently, Kang et al. (2020) and Kang and Protas (2021) applied this method to search for potential singularities in 3D Navier-Stokes flows based on some classical conditional regularity results. Highlights of this more than decade-long research program are summarized in the review paper by Protas (2022). The present investigation represents a first application of this framework to an inviscid problem.

Guided by the local well-posedness result in Theorem 1.1, we aim to find an initial condition  $\boldsymbol{\eta} \in H^m$  subject to certain constraints, such that the  $H^m$  norm of the corresponding solution of the Euler system (1.1) is maximized at a prescribed time  $T$ . The desired initial conditions are thus found as local maximizers of a constrained PDE optimization problem with the square of the  $H^m$  (semi)norm used as the objective functional where for concreteness we set  $m = 3$ . We solve this optimization problem for different time intervals  $[0, T]$  using a Riemannian conjugate gradient method (Absil et al., 2008), where the gradient is conveniently computed from solutions of a suitably-defined adjoint system. Both the Euler system (1.1) and the adjoint system as well as different diagnostic quantities are approximated numerically using pseudospectral methods.

In analogy to the work of Fehn et al. (2022); Guo et al. (2022), we adopt an indirect approach to distinguish between regular and singular evolution based on resolution refinement. When solving the optimization problem on a “short” time interval  $[0, T]$ , if the objective functional approximated using different resolutions converges to a finite value as the resolution is refined, then we conclude the Euler system (1.1) is well-posed on this short interval. However, when the interval  $[0, T]$  is “long”, presumably longer than the minimum time of existence guaranteed by Theorem 1.1, the objective functional evaluated at the optimal solutions may diverge upon resolution refinements. Here “short” and “long” times are defined in relation to the interval of local existence guaranteed by Theorem 1.1. More specifically, a “short” time is assumed to be within that interval, whereas a “long” time is outside. Theorem 1.1 does not provide a precise numerical value for the interval of local existence and in practice, based on numerical experiments, we use  $T = 25$  and  $T = 75$  for the short and long optimization time windows. We do in fact observe these two distinct behaviors and conclude that in the latter scenario the divergence of the objective functional on the long time interval  $[0, 75]$  may signal a potential singularity formation in the flow. Although a definitive conclusion cannot be drawn due to numerical limitations, the behavior of different diagnostic quantities does not contradict the possibility of a singularity formation. The corresponding flow features two colliding vortex rings and while these flow structures are quite deformed, the flow does exhibit certain nontrivial symmetries. In particular, the region in the flow where the potential singularity may occur is nearly axisymmetric.

The structure of the paper is as follows: in Section 2 we formulate an optimization problem designed to elucidate the most extreme behavior possible in an Euler flow and in Section 3 we describe a Riemannian gradient-based approach we use to solve this problem together with its numerical discretization; the extreme flows found by the optimization algorithm on “short” and “long” time intervals are discussed in Section 4; finally, conclusions and outlook are deferred to Section 5.

## 2 Optimization problem

Before introducing the optimization problem, let us first define the function space in which its solutions will be sought. We begin by defining the norm in the Sobolev space  $H^m(\mathbb{T}^3)$  as (Adams and Fournier, 2005)

$$\|\mathbf{u}\|_{H^m} := \left[ \sum_{\mathbf{j} \in \mathbb{Z}^3} (1 + |2\pi\mathbf{j}|^2)^m |\hat{\mathbf{u}}_{\mathbf{j}}|^2 \right]^{1/2}, \quad m \in \mathbb{R}, \quad (2.1)$$

where  $\hat{\mathbf{u}}_{\mathbf{j}}$  is the Fourier coefficient of  $\mathbf{u}$  corresponding to the wavevector  $\mathbf{k} := 2\pi\mathbf{j} = [2\pi j_1, 2\pi j_2, 2\pi j_3]$ . The corresponding homogeneous seminorm, denoted  $\|\cdot\|_{\dot{H}^m}$ , is obtained from (2.1) by dropping the constant ( $\mathbf{j}$ -independent) terms. For simplicity, we will hereafter refer to it as the  $H^m$  seminorm.

### 2.1 Functional setting

Since the Euler system (1.1) is locally well posed in  $H^m(\mathbb{T}^3)$ ,  $m > 5/2$ , cf. Theorem 1.1, it may appear natural to look for optimal initial data  $\boldsymbol{\eta}$  in that space. However, we are interested in finite-time singularities potentially arising in classical solutions, whereas initial conditions constructed in such spaces will in general not be smooth or real-analytic. Moreover, solving the Euler system (1.1) with such initial data would not allow us to benefit from the exponential convergence of the pseudospectral methods used in this study, cf. Section 3.3.1. We will thus consider an extended Gevrey space  $G^\sigma$  with  $\sigma > 0$  of real-analytic functions defined on  $\mathbb{T}^3$  and will endow it with the inner product

$$\begin{aligned} \forall \mathbf{v}, \mathbf{u} \in G^\sigma, \quad \langle \mathbf{v}, \mathbf{u} \rangle_{G^\sigma} &:= \sum_{\mathbf{j} \in \mathbb{Z}^3} (1 + |2\pi\mathbf{j}|^2)^m e^{4\pi\sigma|\mathbf{j}|} \hat{\mathbf{v}}_{\mathbf{j}} \cdot \overline{\hat{\mathbf{u}}_{\mathbf{j}}} \\ &= \int_{\mathbb{T}^3} (1 + |D|^2)^m e^{2\sigma|D|} \mathbf{v} \cdot \mathbf{u} \, d\mathbf{x}, \end{aligned} \quad (2.2)$$

where overbar denotes complex conjugation, whereas the operators  $|D|$  and  $e^{\sigma|D|}$  are defined via

$$\left[ \widehat{|D|\mathbf{v}} \right]_{\mathbf{j}} := 2\pi|\mathbf{j}| \hat{\mathbf{v}}_{\mathbf{j}}, \quad \left[ \widehat{e^{\sigma|D|}\mathbf{v}} \right]_{\mathbf{j}} := e^{2\pi\sigma|\mathbf{j}|} \hat{\mathbf{v}}_{\mathbf{j}}. \quad (2.3)$$

In the setting of our problem, the Gevrey space can be regarded a linear subspace of the Sobolev space  $H^m(\mathbb{T}^3)$ , i.e.,

$$G^\sigma := \left\{ \mathbf{v} \in H^m(\mathbb{T}^3) : \|\mathbf{v}\|_{G^\sigma} = \langle \mathbf{v}, \mathbf{v} \rangle_{G^\sigma}^{1/2} < \infty \right\}, \quad m > \frac{5}{2}, \quad \sigma > 0. \quad (2.4)$$

**Remark 2.1** *It follows from definitions (2.2) and (2.4) that the Gevrey spaces have the property*

$$G^{\sigma_2} \subset G^{\sigma_1} \subset G^0 = H^m, \quad 0 < \sigma_1 < \sigma_2. \quad (2.5)$$

*Our strategy for choosing the value of  $\sigma$  will be discussed in Section 4.1.*

Since the initial condition  $\boldsymbol{\eta}$  in system (1.1) needs to be divergence-free and the quantity  $\int_{\mathbb{T}} \boldsymbol{\eta} d\mathbf{x}$  is an invariant of motion, we introduce the following subspace in which optimal initial conditions will be sought

$$V := \{\mathbf{v} \in G^\sigma : \nabla \cdot \mathbf{v} = 0, \quad \int_{\mathbb{T}^3} \mathbf{v} d\mathbf{x} = \mathbf{0}\}. \quad (2.6)$$

The Gevrey regularity is closely related to the analyticity of complex extensions of functions in  $G^\sigma$ , i.e.,  $\mathbf{u}(\mathbf{z}) := \mathbf{u}(\mathbf{x} + i\mathbf{y})$ , where  $i := \sqrt{-1}$ . If  $\mathbf{u} \in G^\sigma$  can be extended to a strip  $S_\delta := \{\mathbf{z} = [z_1, z_2, z_3]^T \in \mathbb{C}^3 : |\operatorname{Im}(z_1)| + |\operatorname{Im}(z_2)| + |\operatorname{Im}(z_3)| < \delta\}$ , so that  $\mathbf{u}(\mathbf{z})$  does not have any singularities in  $S_\delta$ , then the largest such value of  $\delta$  is called the width of the analyticity strip and we have  $0 < \sigma \leq \delta$ . Furthermore, if  $\mathbf{u} = \mathbf{u}(t)$  is a smooth time-dependent solution of the Euler system (1.1), then the width of the analyticity strip is a function of time,  $\delta = \delta(t)$ .

As regards the analyticity of solutions of the Euler system (1.1), among related works we mention the study by Bardos and Benachour (1977) which showed that if the initial data  $\boldsymbol{\eta}$  is analytic, the solution  $\mathbf{u}(t; \boldsymbol{\eta})$  also remains analytic as long as it is well defined in a certain Hölder space. The relation between the BKM condition (1.2) and the Gevrey regularity was investigated by Kukavica and Vicol (2009) who obtained lower bounds on  $\delta(t)$  proportional to  $\exp\left(-\int_0^t \|\nabla \mathbf{u}(\cdot, s)\|_{L^\infty} ds\right)$ . The width of the analyticity strip  $\delta(t)$  can be conveniently estimated from the Fourier spectrum of the solution  $\mathbf{u}(t)$  (Sulem et al., 1983) and is often used as a regularity indicator whose vanishing implies a singularity formation in numerical computations of Euler flows (Bustamante and Brachet, 2012).

## 2.2 Statement of the optimization problem

Motivated by the local existence result in Theorem 1.1, the goal of our optimization-based formulation is to construct initial data  $\boldsymbol{\eta}$  with a prescribed  $H^m$ ,  $m > 5/2$ , norm, such that at a given time  $T > 0$ , the corresponding solution  $\mathbf{u}(T; \boldsymbol{\eta})$  of the Euler system (1.1) has the largest possible  $H^m$  norm. To fix attention, we will hereafter use  $m = 3$ . Furthermore, since we consider zero-mean initial conditions, cf. (2.6), without loss of generality, we can use the  $H^3$  seminorm instead of the full  $H^3$  norm as this will make the optimization problem more similar to the problem considered by Kang et al. (2020).

We define the objective functional  $\Phi_T : V \rightarrow \mathbb{R}^+$  as

$$\Phi_T(\boldsymbol{\eta}) := \|\mathbf{u}(T; \boldsymbol{\eta})\|_{\dot{H}^3}^2, \quad (2.7)$$

where  $\mathbf{u}(T; \boldsymbol{\eta})$  is the solution of the Euler system (1.1) obtained with the initial condition  $\boldsymbol{\eta} \in V$ . System (1.1) possesses a scaling property such that if  $\{\mathbf{u}(\mathbf{x}, t), p(\mathbf{x}, t)\}$  is a solution, then for any  $\lambda > 0$ ,

$$\left\{ \mathbf{u}^\lambda(\mathbf{x}, t) := \lambda \mathbf{u}(\mathbf{x}, \lambda t), \quad p^\lambda(\mathbf{x}, t) := \lambda^2 p(\mathbf{x}, \lambda t) \right\} \quad (2.8)$$

is also a solution. Hence, for any nonzero initial condition  $\boldsymbol{\eta}$ , we have the identity

$$\Phi_T(\boldsymbol{\eta}) = \|\boldsymbol{\eta}\|_{\dot{H}^3}^2 \Phi_{\|\boldsymbol{\eta}\|_{\dot{H}^3} T} \left( \frac{\boldsymbol{\eta}}{\|\boldsymbol{\eta}\|_{\dot{H}^3}} \right). \quad (2.9)$$

Therefore, we can restrict our discussion to initial conditions with unit  $\dot{H}^3$  seminorm which belong to a closed manifold  $\mathcal{M}_1 \subset V$  defined as

$$\mathcal{M}_1 = \{\mathbf{v} \in V : \|\mathbf{v}\|_{\dot{H}^3} = 1\}. \quad (2.10)$$

Thus, we arrive at the following optimization problem

**Problem 2.2** *Given  $T \in \mathbb{R}_+$ , find*

$$\tilde{\boldsymbol{\eta}}_T = \operatorname{argmax}_{\boldsymbol{\eta} \in \mathcal{M}_1} \Phi_T(\boldsymbol{\eta}). \quad (2.11)$$

Flows corresponding to optimal initial conditions  $\tilde{\boldsymbol{\eta}}_T$  are referred to as “extreme”. Since a priori we do not know if a singularity may appear in Euler flows on a given time interval  $[0, T]$ , we solve the optimization problem for increasing values of  $T$  and deduce whether a singularity may occur inside the interval  $[0, T]$  by performing resolution refinement as discussed in detail in Section 4. If the time window  $[0, T]$  falls within the interval of local existence guaranteed by Theorem 1.1, then for any  $\boldsymbol{\eta} \in \mathcal{M}_1$ , we expect  $\Phi_T(\boldsymbol{\eta})$  to be finite such that it will remain bounded upon resolution refinement. On the other hand, if there exists an  $\boldsymbol{\eta} \in \mathcal{M}_1$ , which will lead to a finite-time blow-up inside a sufficiently long time interval  $[0, T]$ , we anticipate  $\Phi_T(\boldsymbol{\eta})$  to diverge as the resolution is refined.

### 3 Solution approach

We solve Problem 2.2 using a Riemannian conjugate gradient approach which is a modification of a gradient ascent method given by the iterative relation

$$\boldsymbol{\eta}_T^{(n+1)} = \boldsymbol{\eta}_T^{(n)} + \tau_n \nabla \Phi_T \left( \boldsymbol{\eta}_T^{(n)} \right), \quad \boldsymbol{\eta}_T^{(0)} = \boldsymbol{\eta}_0, \quad n = 0, 1, \dots, \quad (3.1)$$

where  $\nabla \Phi_T \left( \boldsymbol{\eta}^{(n)} \right)$  is the gradient of the objective functional  $\Phi_T(\boldsymbol{\eta})$  evaluated at the element  $\boldsymbol{\eta}_T^{(n)}$ ,  $\tau_n$  is the step size along the gradient direction and  $\boldsymbol{\eta}_0$  is the initial guess. A local maximizer  $\tilde{\boldsymbol{\eta}}_T$  of Problem 2.2 can then be found as the limit  $\tilde{\boldsymbol{\eta}}_T = \lim_{n \rightarrow \infty} \boldsymbol{\eta}_T^{(n)}$ , such that

$$\Phi_T(\tilde{\boldsymbol{\eta}}_T) = \lim_{n \rightarrow \infty} \Phi_T \left( \boldsymbol{\eta}_T^{(n)} \right) = \max_{\boldsymbol{\eta} \in \mathcal{M}_1} \Phi_T(\boldsymbol{\eta}) =: \tilde{\Phi}_T; \boldsymbol{\eta}_0. \quad (3.2)$$

Since our optimization problem is non-convex, the sequence constructed in (3.1) may converge to different local maximizers depending on the initial guess  $\boldsymbol{\eta}_0$ . Therefore, we use the subscript  $\boldsymbol{\eta}_0$  on the RHS in (3.2) to indicate the dependence of the local maximizer on the initial guess.

In the spirit of the “optimize-then-discretize” paradigm (Gunzburger, 2003), we first formulate our approach in the infinite-dimensional (continuous) setting and then discretize the resulting relations in numerical computations. A key element of the iterative procedure (3.1) is the evaluation of the gradient  $\nabla \Phi_T(\boldsymbol{\eta})$ , which is based on solving a suitably-defined adjoint system backwards in time as discussed in Section 3.1. The Riemannian conjugate gradient method, which accelerates the gradient ascent method (3.1) for problems defined on smooth manifolds such as  $\mathcal{M}_1$ , is introduced in Section 3.2, whereas numerical techniques used to discretize the problem are briefly discussed in Section 3.3.1. Finally, different initial guesses we use are listed in Section 3.3.2 and in Section 3.3.3 we describe the diagnostic quantities that will be analyzed.

### 3.1 Evaluation of the gradient

To compute the gradient  $\nabla\Phi_T(\boldsymbol{\eta})$  of the objective functional in (3.1), we first introduce the Gâteaux (directional) differential  $\Phi'_T(\boldsymbol{\eta}; \boldsymbol{\eta}') : V \times V \rightarrow \mathbb{R}$

$$\Phi'_T(\boldsymbol{\eta}; \boldsymbol{\eta}') := \lim_{\epsilon \rightarrow 0} \frac{1}{\epsilon} [\Phi_T(\boldsymbol{\eta} + \epsilon\boldsymbol{\eta}') - \Phi_T(\boldsymbol{\eta})], \quad (3.3)$$

which represents the variation of the objective functional  $\Phi_T(\boldsymbol{\eta})$  resulting from applying an infinitesimal perturbation proportional to  $\boldsymbol{\eta}' \in V$  to the initial condition  $\boldsymbol{\eta}$ . Fixing the first argument of  $\Phi'_T(\boldsymbol{\eta}; \boldsymbol{\eta}')$ , we can view the Gâteaux differential (3.3) as a bounded linear functional on  $V$ . Therefore, we can define  $\nabla\Phi_T(\boldsymbol{\eta})$  using the Riesz representation theorem (Luenberger, 1969) in terms of the inner product on  $G^\sigma$ , cf. (2.4), as

$$\Phi'_T(\boldsymbol{\eta}; \boldsymbol{\eta}') = \langle \nabla\Phi_T(\boldsymbol{\eta}), \boldsymbol{\eta}' \rangle_{G^\sigma}, \quad \boldsymbol{\eta}, \boldsymbol{\eta}' \in V. \quad (3.4)$$

The Gâteaux differential can be evaluated by substituting (2.7) into (3.3), which yields

$$\Phi'_T(\boldsymbol{\eta}; \boldsymbol{\eta}') = 2 \langle \mathbf{u}(\cdot, T), \mathbf{u}'(\cdot, T) \rangle_{\dot{H}^3} = 2 \langle |D|^6 \mathbf{u}(\cdot, T), \mathbf{u}'(\cdot, T) \rangle_{L^2}. \quad (3.5)$$

Here  $\mathbf{u}'(\mathbf{x}, t)$  is the solution of the linearization of the Euler system (1.1) around its solution  $\mathbf{u}(\mathbf{x}, t; \boldsymbol{\eta})$ , which is defined by

$$\begin{aligned} \mathcal{L} \begin{bmatrix} \mathbf{u}' \\ p' \end{bmatrix} &:= \begin{bmatrix} \partial_t \mathbf{u}' + \mathbf{u}' \cdot \nabla \mathbf{u} + \mathbf{u} \cdot \nabla \mathbf{u}' + \nabla p' \\ \nabla \cdot \mathbf{u}' \end{bmatrix} = \begin{bmatrix} \mathbf{0} \\ 0 \end{bmatrix}, \\ \mathbf{u}'(\mathbf{x}, 0) &= \boldsymbol{\eta}'(\mathbf{x}), \end{aligned} \quad (3.6)$$

where  $\boldsymbol{\eta}'$  is the perturbation of the initial condition and  $p'(\mathbf{x}, t)$  is the corresponding pressure perturbation.

We note, however, that the expression (3.5) for the Gâteaux differential is not yet consistent with the Riesz representation form (3.4), since the perturbation  $\boldsymbol{\eta}'$  of the initial condition does not appear in it explicitly, but is instead “hidden” in the initial condition of the linearized problem (3.6). In order to transform expression (3.5) into the required Riesz representation form, where the perturbation  $\boldsymbol{\eta}'$  appears explicitly as a linear factor, we introduce the adjoint states  $\{\mathbf{u}^* : \mathbb{T}^3 \times [0, T] \rightarrow \mathbb{R}^3, p^* : \mathbb{T}^3 \times [0, T] \rightarrow \mathbb{R}\}$  and the following duality-pairing relation

$$\begin{aligned} \left( \mathcal{L} \begin{bmatrix} \mathbf{u}' \\ p' \end{bmatrix}, \begin{bmatrix} \mathbf{u}^* \\ p^* \end{bmatrix} \right) &:= \int_0^T \int_{\mathbb{T}^3} \mathcal{L} \begin{bmatrix} \mathbf{u}' \\ p' \end{bmatrix} \cdot \begin{bmatrix} \mathbf{u}^* \\ p^* \end{bmatrix} d\mathbf{x} dt \\ &= \left( \begin{bmatrix} \mathbf{u}' \\ p' \end{bmatrix}, \mathcal{L}^* \begin{bmatrix} \mathbf{u}^* \\ p^* \end{bmatrix} \right) + \int_{\mathbb{T}^3} \mathbf{u}'(\mathbf{x}, T) \cdot \mathbf{u}^*(\mathbf{x}, T) d\mathbf{x} \\ &\quad - \int_{\mathbb{T}^3} \boldsymbol{\eta}'(\mathbf{x}) \cdot \mathbf{u}^*(\mathbf{x}, 0) d\mathbf{x} \\ &= 0. \end{aligned} \quad (3.7)$$

Here “ $\cdot$ ” denotes the usual Euclidean inner product on  $\mathbb{R}^4$  and  $\mathcal{L}^*$  is the *adjoint* operator defined in terms of the following system, which is obtained by performing integration by parts



with respect to both space and time in (3.7)

$$\mathcal{L}^* \begin{bmatrix} \mathbf{u}^* \\ p^* \end{bmatrix} := \begin{bmatrix} -\partial_t \mathbf{u}^* - (\nabla \mathbf{u}^* + (\nabla \mathbf{u}^*)^T) \mathbf{u} - \nabla p^* \\ -\nabla \cdot \mathbf{u}^* \end{bmatrix} = \begin{bmatrix} \mathbf{0} \\ 0 \end{bmatrix}, \quad (3.8)$$

$$\mathbf{u}^*(\mathbf{x}, T) = 2|D|^6 \mathbf{u}(\mathbf{x}, T).$$

We remark that system (3.8) is a *terminal-value* problem and as such has to be integrated backwards in time. We also note that the spatial mean of its solutions is conserved during the time evolution and therefore we have

$$\int_{\mathbb{T}^3} \mathbf{u}^*(\mathbf{x}, T) \, d\mathbf{x} = \int_{\mathbb{T}^3} \mathbf{u}^*(\mathbf{x}, 0) \, d\mathbf{x} = 0. \quad (3.9)$$

Combining (3.4), (3.5), (3.7) and (3.8), we have

$$\Phi'_T(\boldsymbol{\eta}; \mathbf{u}'_0) = \int_{\mathbb{T}^3} \mathbf{u}'(\mathbf{x}, T) \cdot \mathbf{u}^*(\mathbf{x}, T) \, d\mathbf{x} = \int_{\mathbb{T}^3} \mathbf{u}'_0(\mathbf{x}) \cdot \mathbf{u}^*(\mathbf{x}, 0) \, d\mathbf{x} = \langle \nabla \Phi_T(\boldsymbol{\eta}), \boldsymbol{\eta}' \rangle_{G^\sigma}. \quad (3.10)$$

Using the definition of the Gevrey inner product (2.2) in the last equality above, we obtain

$$\begin{aligned} \langle \nabla \Phi_T(\boldsymbol{\eta}), \boldsymbol{\eta}' \rangle_{G^\sigma} &= \int_{\mathbb{T}^3} \mathbf{u}^*(\mathbf{x}, 0) \cdot \boldsymbol{\eta}'(\mathbf{x}) \, d\mathbf{x} \\ &= \int_{\mathbb{T}^3} (1 + |D|^2)^3 e^{2\sigma|D|} \left[ (1 + |D|^2)^{-3} e^{-2\sigma|D|} \mathbf{u}^*(\mathbf{x}, 0) \right] \cdot \boldsymbol{\eta}'(\mathbf{x}) \, d\mathbf{x} \\ &= \left\langle (1 + |D|^2)^{-3} e^{-2\sigma|D|} \mathbf{u}^*(\cdot, 0), \boldsymbol{\eta}'(\cdot) \right\rangle_{G^\sigma}, \end{aligned} \quad (3.11)$$

which allows us to identify the gradient as

$$\nabla \Phi_T(\boldsymbol{\eta}) = (1 + |D|^2)^{-3} e^{-2\sigma|D|} \mathbf{u}^*(0). \quad (3.12)$$

In summary, evaluation of this expression requires the solution of the adjoint system (3.8), which depends on the solution of the Euler system (1.1) with the initial condition  $\boldsymbol{\eta}$ .

### 3.2 Riemannian conjugate gradient method

For any  $\boldsymbol{\eta} \in \mathcal{M}_1$ ,  $\boldsymbol{\eta} + \tau \nabla \Phi_T(\boldsymbol{\eta})$  given by (3.1) is divergence-free but does not necessarily have a unit  $\dot{H}^3$  seminorm and thus will not in general belong to  $\mathcal{M}_1$ . In order to enforce this constraint and accelerate iterations, we use a Riemannian conjugate gradient method that consists of three steps: first, we project the gradient  $\nabla \Phi_T(\boldsymbol{\eta})$  onto the tangent space to  $\mathcal{M}_1$  at  $\boldsymbol{\eta}$ , then perform a suitable *vector transport* operation in order to construct a Riemannian conjugate ascent direction using the previous search direction and, finally, retract the resulting state back to the constraint manifold  $\mathcal{M}_1$ . An analogous approach was employed by (Danaila and Protas, 2017) to solve an infinite-dimensional minimization problem with a similar structure arising in quantum fluids.

We first define the tangent space to  $\mathcal{M}_1$  at  $\mathbf{v}$  as

$$\mathcal{T}_{\mathbf{v}} \mathcal{M}_1 = \left\{ \mathbf{z} \in V : \langle \mathbf{v}, \mathbf{z} \rangle_{\dot{H}^3} = 0 \right\}, \quad (3.13)$$

where the last condition represents the Gâteaux differential of the constraint  $\|\mathbf{v}\|_{\dot{H}^3} = 1$ . For any  $z \in \mathcal{T}_v \mathcal{M}_1$ , this condition can be expressed as

$$\begin{aligned} \langle \mathbf{v}, z \rangle_{\dot{H}^3} &= \int_{\mathbb{T}^3} |D|^3 \mathbf{v} \cdot |D|^3 z \, dx \\ &= \int_{\mathbb{T}^3} (1 + |D|^2)^3 e^{2\sigma|D|} \left( (1 + |D|^2)^{-3} e^{-2\sigma|D|} |D|^6 \mathbf{v} \right) \cdot z \, dx \\ &= \left\langle (1 + |D|^2)^{-3} e^{-2\sigma|D|} |D|^6 \mathbf{v}, z \right\rangle_{G^\sigma} = 0. \end{aligned} \quad (3.14)$$

Thus, at each point  $\mathbf{v} \in \mathcal{M}_1$ , the tangent space  $\mathcal{T}_v \mathcal{M}_1$  can be characterized using the unit “normal” vector given by

$$\mathbf{n}_v = \frac{(1 + |D|^2)^{-3} e^{-2\sigma|D|} |D|^6 \mathbf{v}}{\| (1 + |D|^2)^{-3} e^{-2\sigma|D|} |D|^6 \mathbf{v} \|_{G^\sigma}} \quad (3.15)$$

which allows us to construct the projection operator  $P_{\mathcal{T}_v \mathcal{M}_1} : V \rightarrow \mathcal{T}_v \mathcal{M}_1$ , cf. figure 1,

$$\forall \mathbf{w} \in V, \quad P_{\mathcal{T}_v \mathcal{M}_1} \mathbf{w} = \mathbf{w} - \langle \mathbf{n}_v, \mathbf{w} \rangle_{G^\sigma} \mathbf{n}_v. \quad (3.16)$$

In addition, we also need to introduce the retraction operator  $R : V \rightarrow \mathcal{M}_1$  which has the form of normalization needed to satisfy the constraint  $\|\mathbf{v}\|_{\dot{H}^3} = 1$  (Absil et al., 2008; Sato, 2021)

$$R(\mathbf{v}) = \frac{\mathbf{v}}{\|\mathbf{v}\|_{\dot{H}^3}}, \quad \mathbf{v} \neq \mathbf{0}. \quad (3.17)$$

In the standard (Euclidean) conjugate gradient approach, the search direction at  $(n+1)$ -th iteration is obtained as a suitable linear combination of the steepest ascent direction (i.e., the gradient) computed at  $(n+1)$ -th iteration and the search direction obtained at  $n$ -th iteration. In the Riemannian setting the difficulty with this approach is that these two directions do not belong to the same linear space and hence cannot be added directly. In order to circumvent this difficulty, we introduce the *vector transport* operation defined as

$$\mathcal{T}\mathcal{M}_1 \oplus \mathcal{T}\mathcal{M}_1 \rightarrow \mathcal{T}\mathcal{M}_1 : (\varphi, \xi) \mapsto \Gamma_\varphi(\xi) \in \mathcal{T}\mathcal{M}_1, \quad (3.18)$$

where  $\mathcal{T}\mathcal{M}_1 = \cup_{\mathbf{v} \in \mathcal{M}_1} \mathcal{T}_v \mathcal{M}_1$  is the tangent bundle on  $\mathcal{M}_1$ , describing how the vector field  $\xi$  is transported along the manifold  $\mathcal{M}_1$  in the direction of  $\varphi$  (Absil et al., 2008). The vector transport provides a map between the tangent spaces  $\mathcal{T}_{\eta_T^{(n)}} \mathcal{M}_1$  and  $\mathcal{T}_{\eta_T^{(n+1)}} \mathcal{M}_1$  obtained at two consecutive iterations, so that algebraic operations can be performed on vectors belonging to these subspaces. It therefore generalizes the concept of the parallel translation to the motion on the manifold. In general, vector transport is defined up to a multiplicative prefactor and can be computed via the differentiated retraction as (Absil et al., 2008)

$$\mathcal{T}_{\varphi_u}(\xi_u) = \frac{d}{dt} R_u(\varphi_u + t\xi_u)|_{t=0} = \frac{1}{\|\mathbf{u} + \varphi_u\|_{\dot{H}^3}} \left[ \xi_u - \frac{\langle \mathbf{u} + \varphi_u, \xi_u \rangle_{\dot{H}^3}}{\|\mathbf{u} + \varphi_u\|_{\dot{H}^3}^2} (\mathbf{u} + \varphi_u) \right], \quad \mathbf{u} \in \mathcal{M}_1 \quad (3.19)$$

Combining the elements introduced above, the Riemannian conjugate gradient approach is given by the iterative relation

$$\boldsymbol{\eta}_T^{(n+1)} = R \left[ \boldsymbol{\eta}_T^{(n)} + \tau_n \mathbf{d}^{(n)} \right], \quad \boldsymbol{\eta}_T^{(0)} = \boldsymbol{\eta}_0, \quad n = 0, 1, \dots, \quad (3.20)$$

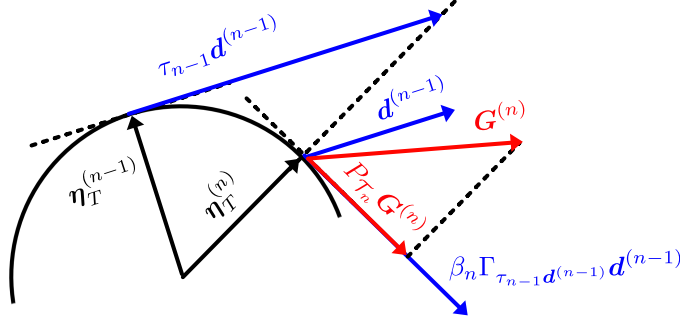


Figure 1: Schematic illustration of the Riemannian conjugate gradient method (3.20).

and is also schematically illustrated in figure 1. Here the search direction  $\mathbf{d}^{(n)}$  is computed as

$$\begin{aligned} \mathbf{d}^{(0)} &= \mathbf{P}_{\mathcal{T}_0} \mathbf{G}^{(0)}, \\ \mathbf{d}^{(n)} &= \mathbf{P}_{\mathcal{T}_n} \mathbf{G}^{(n)} + \beta_n \Gamma_{\tau_{n-1} \mathbf{d}^{(n-1)}} (\mathbf{d}^{(n-1)}), \quad n \geq 1, \end{aligned} \quad (3.21)$$

where  $G^{(n)} := \nabla \Phi_T(\boldsymbol{\eta}^{(n)})$  and  $\mathcal{T}_n := \mathcal{T}_{\boldsymbol{\eta}^{(n)}} \mathcal{M}_1$ . The ‘‘momentum’’ term  $\beta_n$  is chosen to enforce the conjugacy of consecutive search directions and is computed using the Polak-Ribière approach (Nocedal and Wright, 1999)

$$\beta_n = \frac{\left\langle \mathbf{P}_{\mathcal{T}_n} \mathbf{G}^{(n)}, \left( \mathbf{P}_{\mathcal{T}_n} \mathbf{G}^{(n)} - \Gamma_{\tau_{n-1} \mathbf{d}^{(n-1)}} \mathbf{P}_{\mathcal{T}_{n-1}} \mathbf{G}^{(n-1)} \right) \right\rangle_{G^\sigma}}{\left\| \mathbf{P}_{\mathcal{T}_{n-1}} \mathbf{G}^{(n-1)} \right\|_{G^\sigma}^2}. \quad (3.22)$$

The step size  $\tau_n$  in (3.20) is determined by solving the arc-search problem

$$\tau_n = \operatorname{argmax}_{\tau > 0} \left\{ \Phi_T \left( \mathbf{R} \left[ \boldsymbol{\eta}^{(n)} + \tau \mathbf{d}^{(n)} \right] \right) \right\} \quad (3.23)$$

using a suitable derivative-free approach, such as a variant of Brent’s algorithm (Press et al., 1986). Due to the presence of the retraction operator (3.17) in (3.20), the search in (3.23) is performed following a geodesic arc on the manifold  $\mathcal{M}_1$ , this problem can be regarded as a generalization of the more common line search approach (Press et al., 1986).

### 3.3 Numerical methods

#### 3.3.1 Discretization, validation and numerical parameters

In numerical computations, systems (1.1) and (3.8) are discretized in space using a standard pseudospectral Fourier method where derivatives are evaluated in the Fourier space, whereas nonlinear products are computed in the physical space on an uniform grid with  $N$  points in each direction. As regards dealiasing, we use the Gaussian filter proposed by Hou and Li (2007) which is defined in terms of the Fourier multiplier  $\widehat{G}_j := \exp \left\{ -36 \left[ (2|j_1|/N)^{36} + (2|j_2|/N)^{36} + (2|j_3|/N)^{36} \right] \right\}$ . As discussed in Section 4.2, this filter will also serve to prevent the blow-up of the numerical solution after it becomes under-resolved. The resulting system of ordinary differential equations is discretized in time using an explicit fourth-order Runge-Kutta (RK4) method. The

code is parallelized using MPI and the fast Fourier transforms (FFTs) are computed using the parallel version of the software library FFTW (Frigo and Johnson, 2003). We consider four spatial resolutions with  $N^3 = 128^3, 256^3, 512^3, 1024^3$  and the time steps  $\Delta t$  are adjusted to satisfy the stability conditions of the RK4 method. If needed, the resolution used will be denoted with a superscript  $N$ , i.e.,  $\mathbf{u}^N(t)$  represents the numerical solution of the Euler system (1.1) computed with the resolution  $N^3$ , etc. At each iteration in (3.20), the solution  $\mathbf{u}(t)$  of the Euler system (1.1) is needed to construct coefficients in the adjoint system (3.8). For the three smaller resolutions, we store the solutions of (1.1) at discrete time steps so that they can be read directly from files when solving (3.8). However, this is not possible for the resolution of  $1024^3$  due to storage limitations. We get around this difficulty using the time-reversibility of the Euler system (1.1) to evolve this system backwards in time while solving the adjoint system; this allows us to determine the coefficients in the latter system without having to store the entire solution to the former.

The solver for the Euler system (1.1) was validated by verifying the convergence of the numerical solutions to certain exact solutions of (1.1) as we increase the spatial resolution and/or decrease the time step. As regards the accuracy of the evaluation of the gradient  $\nabla\Phi_T(\boldsymbol{\eta})$ , we consider the quantity (Ayala, 2014)

$$\kappa^N(\epsilon) := \frac{\Phi_T^N(\boldsymbol{\eta} + \epsilon\boldsymbol{\eta}') - \Phi_T^N(\boldsymbol{\eta})}{\epsilon \langle \nabla\Phi_T^N(\boldsymbol{\eta}), \boldsymbol{\eta}' \rangle_{G^\sigma}} \quad (3.24)$$

which is the ratio of a finite-difference approximation of the Gâteaux differential (3.3) and its representation in terms of the Riesz representation formula (3.4), both approximated using the resolution  $N^3$ . In theory, we expect that  $\lim_{N \rightarrow \infty} \lim_{\epsilon \rightarrow 0} \kappa^N(\epsilon) = 1$ . However, in numerical computations performed with finite-precision arithmetics,  $\kappa^N(\epsilon)$  will become unbounded as  $\epsilon \rightarrow 0$  due to subtractive cancellation errors in the numerator in (3.24). For intermediate values of  $\epsilon$ , the quantity  $|\kappa^N(\epsilon) - 1|$  is a measure of inaccuracies involved in the computation of  $\Phi_T^N(\boldsymbol{\eta})$  and  $\nabla\Phi_T^N(\boldsymbol{\eta})$  due to approximation errors in the numerical solution of systems (1.1) and (3.8). In our validation tests, we observed that, as expected,  $|\kappa^N(\epsilon) - 1|$  is reduced as the discretization parameters  $N$  and  $\Delta t$  are refined.

In computations with the nonlinear conjugate gradient method, it is common to restart the algorithm periodically with a simple gradient step, i.e., by setting  $\beta_n = 0$ , which allows us to improve convergence by getting rid of ineffectual old information (Nocedal and Wright, 1999). In our computations we restart the algorithm (3.20) based on the following two criteria:

- (1)  $n = 20k, k \in \mathbb{Z}_+$ ,
- (2) The search direction  $\mathbf{d}^{(n)}$  fails to be an ascent direction, i.e.,

$$\frac{\langle \mathbf{d}^{(n)}, \text{P}_{\mathcal{T}_n} G^{(n)} \rangle_{G^\sigma}}{\|\mathbf{d}^{(n)}\|_{G^\sigma} \|\text{P}_{\mathcal{T}_n} G^{(n)}\|_{G^\sigma}} < \epsilon_{\text{machine}}, \quad 0 < \epsilon_{\text{machine}} \ll 1. \quad (3.25)$$

Iterations (3.20) are declared converged when the relative change of the objective functional between two consecutive iterations becomes smaller than a specified tolerance  $0 < \text{tol} \ll 1$ ,

i.e., when

$$0 \leq \frac{\tilde{\Phi}_T^N(\boldsymbol{\eta}_T^{(n+1)}) - \tilde{\Phi}_T^N(\boldsymbol{\eta}_T^{(n)})}{\tilde{\Phi}_T^N(\boldsymbol{\eta}_T^{(n)})} < \text{tol.} \quad (3.26)$$

### 3.3.2 Initial guesses

Since Problem 2.2 is non-convex, iterations (3.20) may produce local maximizers which will depend on the initial guess  $\boldsymbol{\eta}_0$ . In numerical computations, we thus consider a variety of different initial guesses listed below, all normalized such that  $\|\boldsymbol{\eta}_0\|_{\dot{H}^3} = 1$ . For simplicity, we use the same notation for the original initial conditions and their normalizations. In each case, we solve Problem 2.2 to obtain an optimal initial condition  $\tilde{\boldsymbol{\eta}}_T$  such that for any given  $T$  the norm  $\|\mathbf{u}(T; \tilde{\boldsymbol{\eta}}_T)\|_{\dot{H}^3}$  is larger than  $\|\mathbf{u}(T; \boldsymbol{\eta}_0)\|_{\dot{H}^3}$  where  $\boldsymbol{\eta}_0$  is each of the following initial guesses.

- (1) The 3D Taylor-Green vortex (Taylor and Green, 1937):

$$\boldsymbol{\eta}_{\text{TG}} := \begin{bmatrix} \sin(2\pi x) \cos(2\pi y) \cos(2\pi z) \\ -\cos(2\pi x) \sin(2\pi y) \cos(2\pi z) \\ 0 \end{bmatrix}. \quad (3.27)$$

The Taylor-Green vortex has been widely used as a candidate for potential blow-up in Euler flows, however, it is still an open question whether this initial condition can indeed lead to a singularity formation in a finite time (Cichowlas and Brachet, 2005; Bustamante and Brachet, 2012; Fehn et al., 2022). We mention that the time windows  $[0, T]$  considered in this paper are much shorter than the times when a potentially singular behavior was observed in these earlier studies.

- (2) Random initial condition:

$$\boldsymbol{\eta}_{\text{rand}} := \text{P}_L \mathbf{v}_{\text{rand}} := \mathbf{v}_{\text{rand}} - \nabla \Delta^{-1}(\nabla \cdot \mathbf{v}_{\text{rand}}), \quad (3.28)$$

where  $\text{P}_L$  is the Leray projector (Majda and Bertozzi, 2002) with the property that for any  $\mathbf{w} \in H^1(\mathbb{T}^3)$ ,  $\nabla \cdot (\text{P}_L \mathbf{w}) = 0$ , and  $\mathbf{v}_{\text{rand}}$  is given by

$$\mathbf{v}_{\text{rand}} = \begin{bmatrix} v_1 \\ v_2 \\ v_3 \end{bmatrix} = \begin{bmatrix} \sum_{|j_1|+|j_2|+|j_3| \leq N_0} e^{-|j|/(4\pi)} e^{i2\pi\theta_1(j_1)} e^{i2\pi\mathbf{j} \cdot \mathbf{x}} + c.c. \\ \sum_{|j_1|+|j_2|+|j_3| \leq N_0} e^{-|j|/(4\pi)} e^{i2\pi\theta_2(j_2)} e^{i2\pi\mathbf{j} \cdot \mathbf{x}} + c.c. \\ \sum_{|j_1|+|j_2|+|j_3| \leq N_0} e^{-|j|/(4\pi)} e^{i2\pi\theta_3(j_3)} e^{i2\pi\mathbf{j} \cdot \mathbf{x}} + c.c. \end{bmatrix}, \quad (3.29)$$

in which  $\theta_1, \theta_2$  and  $\theta_3$  are  $N_0$ -dimensional random variables with uniform distributions on  $[0, 1]^{N_0}$ . In practice, we choose  $N_0 = 64$  and emphasize that in contrast to the unimodal Taylor-Green vortex (3.27), the random initial condition (3.28) has energy distributed over Fourier coefficients with wavevectors within the shell of radius  $2\pi N_0$ .

- (3) Kerr's initial condition (Kerr, 1993; Hou and Li, 2006):

$$\boldsymbol{\eta}_{\text{K}} := \nabla \times (|D|^{-2} \boldsymbol{\omega}_{\text{K}}) \quad (3.30)$$

which represents two perturbed anti-parallel vortex tubes located symmetrically with respect to the  $xy$ -plane such that  $\boldsymbol{\omega}_K(x, y, z) = -\boldsymbol{\omega}_K(x, y, -z)$ . The vorticity of the vortex tube above the  $xy$ -plane is given by

$$\boldsymbol{\omega}_K = 8G\omega(r)[\omega_1, \omega_2, \omega_3]^T, \quad (3.31)$$

where  $G$  is a Fourier filter defined by  $\hat{G}_j = \exp(-0.05(j_1^4 + j_2^4 + j_3^4))$  and

$$\omega(r) = \begin{cases} \exp\left[\frac{-r^2}{1-r^2} + r^4(1+r^2+r^4)\right], & r < 1, \\ 0, & r \geq 1, \end{cases} \quad r = \frac{1}{R}\sqrt{[x-x(s)]^2 + [z-z(s)]^2},$$

$$x(s) = \delta_x \cos(\pi s/L_x), \quad z(s) = z_0,$$

$$s(y) = y_2 + L_y \delta_{y_1} \sin(\pi y_2/L_y), \quad y_2(y) = 4\pi y + L_y \delta_{y_2} \sin(\pi(4\pi y)/L_y),$$

$$\omega_1 = -\frac{\pi \delta_x}{L_x} [1 + \pi \delta_{y_2} \cos(\pi(4\pi y)/L_y)] \cdot [1 + \pi \delta_{y_1} \cos(\pi y_2/L_y)] \sin(\pi s/L_x),$$

$$\omega_2 = 1, \quad \omega_3 = 0. \quad (3.32)$$

We choose the same parameters as Hou and Li (2006), i.e.,

$$\delta_{y_1} = 0.5, \delta_{y_2} = 0.4, \delta_x = -1.6, z_0 = 1.57, R = 0.75, L_x = L_y = 4\pi, L_z = 2\pi. \quad (3.33)$$

We would like to point out that in Hou and Li (2006), the equations are posed on  $[-2\pi, 2\pi]^3$  rather than  $[-1/2, 1/2]^3$ . We also note that due to a different normalization, the times up to which Kerr (1993); Hou and Li (2006) were able to compute solutions of the Euler system (1.1) with the initial condition  $\boldsymbol{\eta}_K$  correspond to  $t_1 = 108231$  and  $t_2 = 110059$ , respectively, and are significantly longer than the optimization windows considered in this study.

(4) Hou's axisymmetric initial condition (Hou, 2022):

$$\boldsymbol{\eta}_H := Gu_\theta \mathbf{e}_\theta, \quad (3.34)$$

where  $\mathbf{e}_\theta$  is the unit vector in the azimuthal direction of the cylindrical coordinate system and  $u_\theta$  is the angular velocity component given by

$$u_\theta = \begin{cases} r \exp(-r^2/(1-r^2)) \frac{12000(1-r^2)^{18} \sin(2\pi z)}{1+12.5 \sin^2(\pi z)}, & r < 1, \\ 0, & r \geq 1, \end{cases} \quad r = \frac{\sqrt{x^2 + y^2}}{0.9}. \quad (3.35)$$

This initial condition is a ‘‘compactified’’ version of the initial condition originally considered by Hou (2022), where it was defined on a cylindrical domain of unit radius and with a no-flow boundary condition. The results reported by Hou (2022) indicate that the Euler flow on such a bounded domain obtained with the initial condition (3.34) develops a singularity at the origin after a finite, albeit quite long, time.

### 3.3.3 Diagnostic quantities

We analyze numerical solutions of system (1.1) based on the following diagnostic quantities: the  $\dot{H}^3$  seminorm of the velocity field  $\mathbf{u}(t)$ , the  $L^\infty$  norm of the vorticity field  $\boldsymbol{\omega}(t)$  and the width  $\delta(t)$  of the analyticity strip characterizing the velocity field, all of which are functions of time  $t$ .

We approximate  $\|\mathbf{u}(t)\|_{\dot{H}^3}$  and  $\|\boldsymbol{\omega}(t)\|_{L^\infty}$  as

$$\|\mathbf{u}(t)\|_{\dot{H}^3} \approx \sqrt{\sum_{j_1=0}^{N-1} \sum_{j_2=0}^{N-1} \sum_{j_3=0}^{N-1} |2\pi\mathbf{j}|^6 |\hat{\mathbf{u}}_{\mathbf{j}}(t)|^2}, \quad (3.36a)$$

$$\|\boldsymbol{\omega}(t)\|_{L^\infty} \approx \max_{0 \leq j_1, j_2, j_3 < N} |\boldsymbol{\omega}(j_1/N, j_2/N, j_3/N, t)|. \quad (3.36b)$$

The width of the analyticity strip  $\delta(t)$  has been used to diagnose singularity formation in solutions of various PDEs (Sulem et al., 1983), including the 3D Euler equations (1.1) (Bustamante and Brachet, 2012). To approximate it, we first define the energy spectrum of  $\mathbf{u}(\mathbf{x}, t)$  as

$$e(k, t) := \frac{1}{2} \sum_{j \leq |j| < j+1} |\hat{\mathbf{u}}_{\mathbf{j}}(t)|^2, \quad k = 2\pi j, \quad j \in \mathbb{N}, \quad (3.37)$$

such that the kinetic energy of the flow is

$$E(t) := \frac{1}{2} \int_{\mathbb{T}^3} |\mathbf{u}(\mathbf{x}, t)|^2 d\mathbf{x} = \frac{1}{2} \sum_{\mathbf{j} \in \mathbb{Z}^3} |\hat{\mathbf{u}}_{\mathbf{j}}(t)|^2 = \sum_j e(2\pi j, t). \quad (3.38)$$

When  $\mathbf{u}(t)$  is real-analytic and admits an extension to the complex space  $\mathbb{C}^3$ , it can be shown that the energy spectrum (3.37) has the following asymptotic representation as  $k \rightarrow \infty$  (Carrier et al., 2005)

$$e(k, t) = C(t) k^{-n(t)} e^{-2k\delta(t)}, \quad (3.39)$$

where  $C(t)$  is a scaling constant and  $n(t)$  is the order of the singularity nearest to the real line. Clearly, the loss of analyticity and hence the singularity formation are signalled by the vanishing of  $\delta(t)$ . Fixing the time  $t$  and computing the logarithm of (3.39), the parameters  $C(t)$ ,  $n(t)$  and  $\delta(t)$  can be determined by performing a least-squares fit to minimize the error functional

$$\chi(t) := \sum_{k=k_<}^{k_>} [\ln e(k, t) - \ln C(t) + n(t) \ln k + 2k\delta(t)]^2, \quad (3.40)$$

where  $k_< = 4\pi$  and  $k_>$  is determined in a slightly different manner for different time windows  $T$  (details are provided below). Since  $(\ln(k+2\pi) - \ln k)$  decreases as  $k$  grows, the transformed wavenumbers  $\{\ln k, k \in 2\pi\mathbb{N}\}$  are not evenly distributed over the interval  $[\ln k_<, \ln k_>]$ . This makes it difficult to accurately determine the parameter  $n(t)$ , as there are fewer grid points for smaller values of  $k$ . In order to get around this problem, we perform the fit using grid points distributed uniformly over the interval  $[\ln k_<, \ln k_>]$  where the error functional (3.40) is evaluated by performing a linear interpolation of  $e(k, t)$  onto these equispaced points.

## 4 Numerical results

To distinguish between regular and potentially singular evolution, we solve Problem 2.2 on “short” and “long” time intervals  $[0, T]$  and perform a resolution refinement, where optimal initial conditions  $\tilde{\boldsymbol{\eta}}_T^N$  and the corresponding Euler flows  $\mathbf{u}^N(t; \tilde{\boldsymbol{\eta}}_T^N)$  are computed with increasing numerical resolutions  $N^3$ , cf. Section 3.3.1. We add that, based on the characteristic length scale  $L = 1$  (given by the size of the domain  $\Omega$ ) and the “size” of the initial data  $U \sim 1$ , the characteristic time scale of the flow is  $L/U \sim 1$ .

When  $T$  is sufficiently small, such that the Euler system (1.1) is guaranteed by Theorem 1.1 to be well-posed on  $[0, T]$ , we expect that

$$\lim_{N \rightarrow \infty} \Phi_T(\tilde{\boldsymbol{\eta}}_T^N) < \infty, \quad (4.1)$$

i.e., the objective functional (2.7) must remain finite upon resolution refinement.

On the other hand, when  $T$  is large enough such that Theorem 1.1 does not assert the existence of classical solutions on  $[0, T]$  for regular initial data  $\boldsymbol{\eta}$ , the divergence of the objective functional (2.7) upon resolution refinement

$$\lim_{N \rightarrow \infty} \Phi_T(\tilde{\boldsymbol{\eta}}_T^N) = \infty \quad (4.2)$$

would signal the possibility of a singularity formation at some  $t \in [0, T]$ . As we shall see in Section 4.1 and Section 4.2 below, behaviors consistent with (4.1) and (4.2) are in fact observed in solutions of Problem 2.2 obtained with  $T = 25$  and  $T = 75$ , respectively, with the caveat that the limits in (4.1)–(4.2) are extrapolated from four resolutions only ( $N^3 = 128^3, 256^3, 512^3, 1024^3$ ).

### 4.1 Results for $T = 25$

Since solutions of Problem 2.2 depend on the value of the parameter  $\sigma$  defining the Gevrey space via (2.2) and (2.4), we begin by examining the effect of this parameter on these solutions. We solve Problem 2.2 in different Gevrey spaces  $G^\sigma$  with  $\sigma = 10^{-1}, 10^{-2}, \dots, 10^{-5}$  using the resolution  $128^3$  and two initial guesses  $\boldsymbol{\eta}_{\text{TG}}$  and  $\boldsymbol{\eta}_{\text{rand}}$ . The dependence of the value of the objective functional  $\Phi_{25}(\boldsymbol{\eta}^{(n)})$  on the iteration index  $n$  in (3.20) is shown for different  $\sigma$  in figure 2 for the two initial guesses. We observe that as long as  $\sigma$  is sufficiently small ( $\sigma < 10^{-1}$ ), its value does not have an appreciable effect on the maximum attained value  $\tilde{\Phi}_{25}$  of the objective functional. However, this parameter does affect the rate of convergence and smaller values of  $\sigma$  typically result in faster convergence. This can be interpreted in terms of an “effective dimension” of the discrete space used to approximate the optimal initial condition  $\tilde{\boldsymbol{\eta}}_{25}^N$ , which is larger for smaller  $\sigma$  since decreasing the value of this parameter reduces the penalty on the Fourier components of  $\tilde{\boldsymbol{\eta}}_{25}^N$  with large wavenumbers  $|\mathbf{k}|$ . Hereafter we will use  $\sigma = 10^{-5}$  which results in both larger attained values of  $\tilde{\Phi}_{25}$  and faster convergence of iterations in (3.20), cf. figure 2.

Since Problem 2.2 is non-convex, iterations (3.20) may lead to different local maximizers depending on the choice of the initial guess  $\boldsymbol{\eta}$ . To assess this possibility, we solve Problem 2.2 using four initial guesses  $\boldsymbol{\eta}_{\text{TG}}$ ,  $\boldsymbol{\eta}_{\text{rand}}$ ,  $\boldsymbol{\eta}_{\text{K}}$  and  $\boldsymbol{\eta}_{\text{H}}$  introduced in Section 3.3.2 with the resolution  $128^3$ . The results are presented in figures 3(a) and 3(b) where we show, respectively, the value of the objective functional  $\Phi_{25}(\boldsymbol{\eta}^{(n)})$  as a function of the iteration index  $n$  and the energy spectra



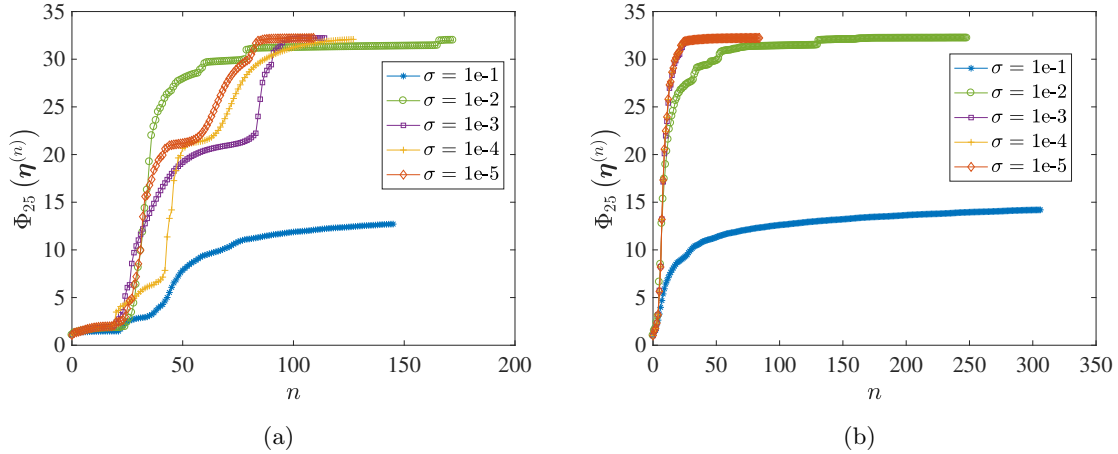


Figure 2: [Short time window,  $T = 25$ ] Dependence of the objective functional  $\Phi_{25}(\boldsymbol{\eta}^{(n)})$  on the iteration index  $n$  for different values of  $\sigma$  when (a)  $\boldsymbol{\eta}_{\text{TG}}$  and (b)  $\boldsymbol{\eta}_{\text{rand}}$  are used as initial guesses in (3.20).

(3.37) of the optimal initial conditions  $\tilde{\boldsymbol{\eta}}_{25}$  obtained with different initial guesses. From the coincidence of the terminal values  $\tilde{\Phi}_{25}$  in figure 3(a) and of the energy spectra  $e(k, 0)$  in figure 3(b) we conclude that an essentially the same optimal initial condition  $\tilde{\boldsymbol{\eta}}_{25}$  is found when the initial guesses  $\boldsymbol{\eta}_{\text{TG}}$ ,  $\boldsymbol{\eta}_{\text{rand}}$  and  $\boldsymbol{\eta}_{\text{H}}$  are used. On the other hand, with the initial guess  $\boldsymbol{\eta}_{\text{K}}$ , a much lower (approximately by a factor of 4) terminal value  $\tilde{\Phi}_{25}$  of the objective functional is found, cf. figure 3(a), which corresponds to an optimal initial condition with less energy in the high-wavenumber part of the spectrum in figure 3(b). The reason for this is that the initial condition  $\boldsymbol{\eta}_{\text{K}}$  is designed to produce a large growth of different diagnostic quantities only after a long time, approximately  $t \approx 110059$  (this value of  $t$  is obtained by rescaling the time when Hou and Li (2006) stopped their computations to account for the normalization  $\|\boldsymbol{\eta}\|_{\dot{H}^3} = 1$  we use in the present study). In the remainder of this subsection we will use  $\boldsymbol{\eta}_{\text{TG}}$  as the initial guess in (3.20), which will allow us to compare our results with the findings of earlier studies of potential singularities in Euler flows that used the Taylor-Green vortex as the initial condition (Bustamante and Brachet, 2012).

As is evident from figure 3(b), calculations performed with the resolution  $128^3$  are not fully resolved since in all cases the optimal initial conditions  $\tilde{\boldsymbol{\eta}}_{25}$  have Fourier coefficients with magnitudes larger than the machine precision for wavenumbers  $|\mathbf{k}| > k_0 := 2\pi\lfloor N/3 \rfloor$ , which results in aliasing errors. To address this issue, we solve Problem 2.2 with increasing resolutions  $N^3 = 256^3, 512^3, 1024^3$ , which is done using the optimal initial condition  $\tilde{\boldsymbol{\eta}}_{25}^N$  as the initial guess for the iteration (3.20) performed with the resolution  $(2N)^3$ . The dependence of the objective functional  $\Phi_{25}^N(\boldsymbol{\eta}^{(n)})$  on the iteration index  $n$  is shown in figure 4(a), where we see that larger values of the objective functional are achieved each time the resolution is refined. We also observe that after each resolution refinement, fewer iterations are needed to achieve convergence; this is because only the Fourier coefficients with high wavenumbers, which represent the fine structures in the flow, need to be adjusted following a resolution refinement. As is evident from figure 4(b), the maximum values of the objective functional  $\tilde{\Phi}_{25}^N$  converge

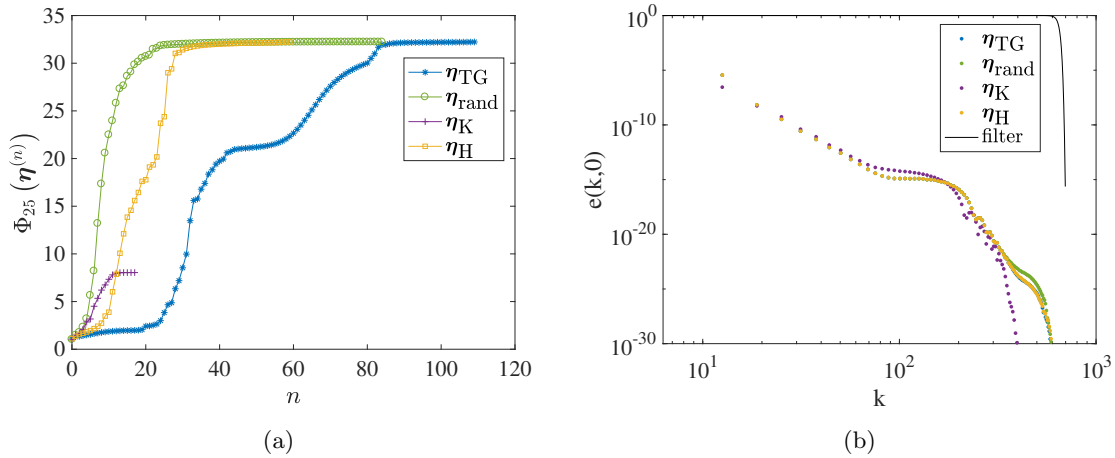


Figure 3: [Short time window,  $T = 25$ ] (a) Dependence of the objective functional  $\Phi_{25}(\eta^{(n)})$  on the iteration index  $n$  and (b) energy spectra (3.37) of the optimal initial conditions  $\tilde{\eta}_{25}^N$  corresponding to different initial guesses  $\eta_{TG}$ ,  $\eta_{rand}$ ,  $\eta_K$  and  $\eta_H$  used in iterations (3.20). In panel (b) the solid line represents the Gaussian filter we use (Hou and Li, 2007).

to a well-defined finite limit as the resolution increases, cf. (4.1).

The energy spectra of the optimal initial conditions  $\tilde{\eta}_{25}^N$  and of the corresponding terminal states  $\mathbf{u}^N(25; \tilde{\eta}_{25}^N)$  are shown in figures 5(a) and 5(b) for different resolutions. These plots indicate that the computations are well resolved with  $N^3 = 1024^3$ . The time evolution of the width  $\delta(t)$  of the analyticity strip and of the corresponding order  $n(t)$  of the singularity are shown for  $N^3 = 512^3, 1024^3$  in figures 6(a) and 6(b), respectively. When determining these parameters by minimizing (3.40) we use  $k_> = \min\{k_0, \sup_{e(k,t) \geq 10^{-30}} k\}$ , i.e., the spectrum was fitted up to the maximum wavenumbers unaffected by aliasing or to wavenumbers at which the magnitude of the Fourier coefficients would drop to the level of the machine precision. The fitting was also terminated whenever  $\delta(t) \leq 0$ . Besides aliasing errors, we use another criterion to gauge the reliability of our computation which is based on  $\delta(t)$ . Following (Brachet et al., 1983; Bustamante and Brachet, 2012), we define a “reliability time”  $T_{rel}$  using the condition

$$\delta(T_{rel}) k_0 = 2 \quad (4.3)$$

and declare the numerical computation trustworthy for times  $t \leq T_{rel}$ , or in other words, as long as  $\delta(t) \geq 2/k_0$ . In figure 6(a) the reliability conditions (4.3) for different resolutions are marked with horizontal lines. The reliability time increases as we increase the resolution and the figure shows that the simulation remains reliable throughout the entire time interval  $[0, 25]$  when  $N = 1024$ , which is consistent with figure 5(b). In figure 6(a),  $\delta(t)$  reveals a mild decrease only near the end of the time window  $[0, 25]$ . These observations further confirm that the extreme Euler flows which correspond to the initial data  $\tilde{\eta}_{25}^N$  obtained as local maximizers of Problem 2.2 for  $T = 25$  remain regular on the interval  $[0, 25]$ .

To close this subsection, in figures 7(a) and 7(b) we compare time evolution of the norms  $\|\mathbf{u}(t)\|_{\dot{H}^3}$  and  $\|\boldsymbol{\omega}(t)\|_{L^\infty}$  in Euler flows corresponding to different initial conditions listed in Section 3.3.2. We see that the growth of  $\|\mathbf{u}(t)\|_{\dot{H}^3}$  is by far the largest in the flow with the

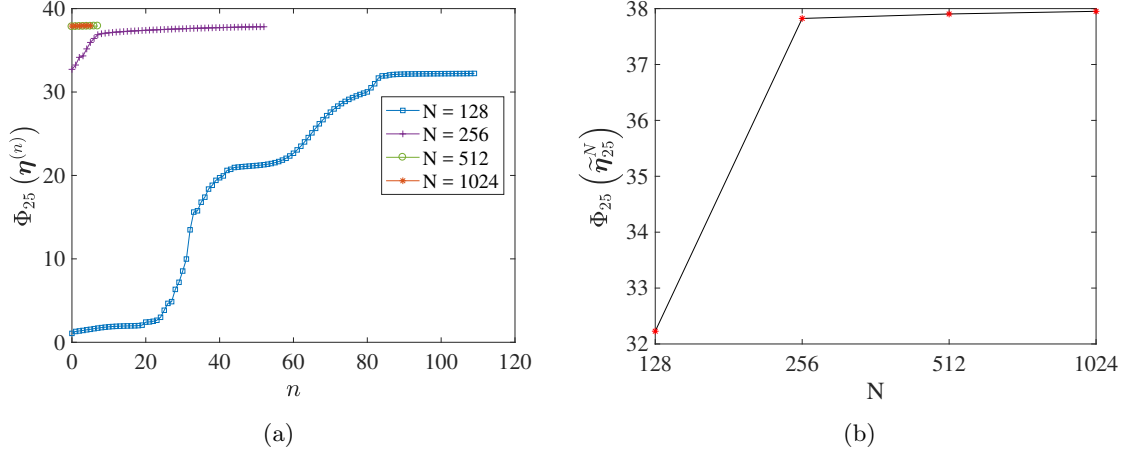


Figure 4: [Short time window,  $T = 25$ ] Dependence of (a) the objective functional  $\Phi_{25}^N(\eta^{(n)})$  on the iteration index  $n$  for different resolutions  $N^3$  and (b) of the corresponding maximum attained values  $\Phi_{25}^N$  of the objective functional on  $N$ .

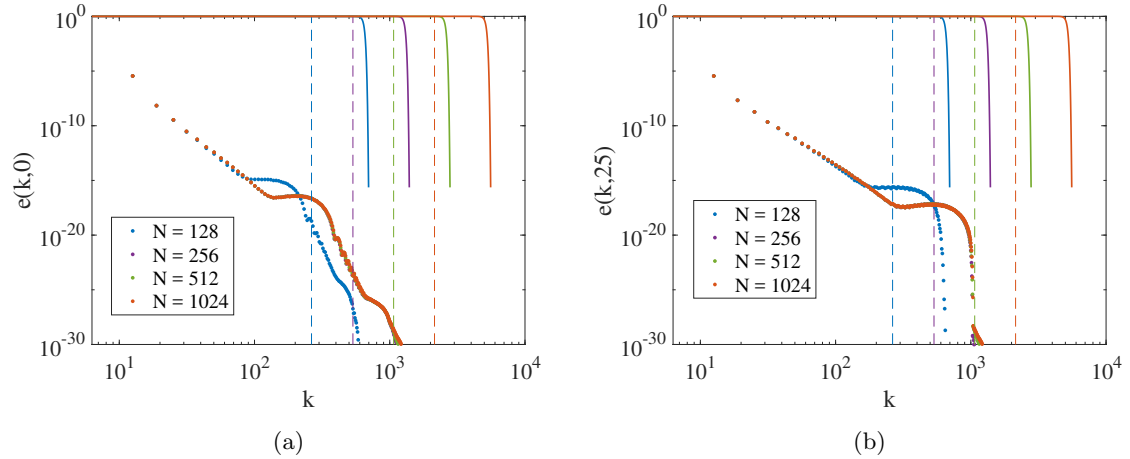


Figure 5: [Short time window,  $T = 25$ ] The energy spectra of (a) the optimal initial conditions  $\tilde{\eta}_{25}^N$  and (b) of the corresponding terminal states  $\mathbf{u}^N(25; \tilde{\eta}_{25}^N)$  obtained for different resolutions  $N^3$ . The solid lines represent the Gaussian filters we use (Hou and Li, 2007) whereas the dashed lines mark the threshold wavenumber  $k_0$  above which aliasing errors occur.

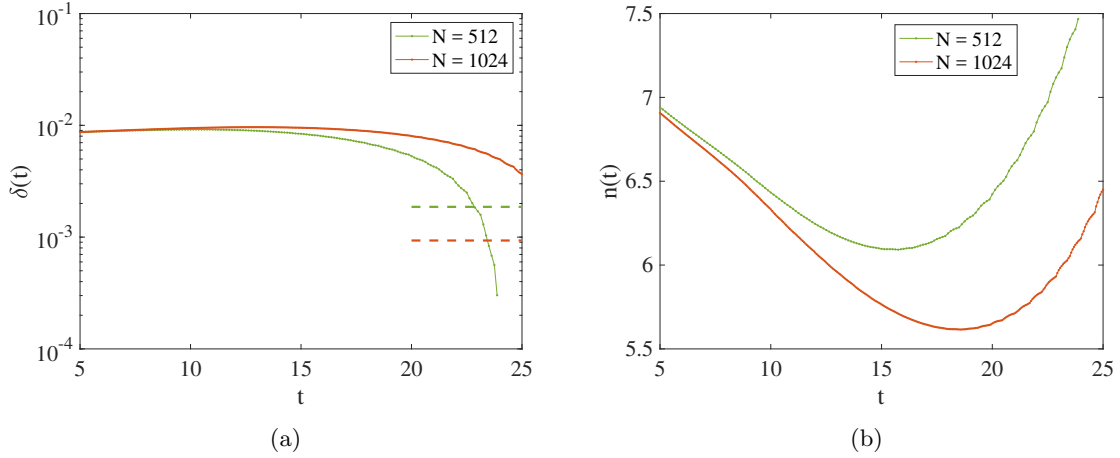


Figure 6: [Short time window,  $T = 25$ ] Dependence of (a) the width  $\delta(t)$  of the analyticity strip and (b) the corresponding order  $n(t)$  of the singularity, cf. (3.39), on time  $t \in [0, 25]$  in the extreme flows computed with resolutions  $N^3 = 512^3, 1024^3$ . In (a) the horizontal lines represent the reliability condition (4.3) corresponding to different resolutions.

optimal initial condition  $\tilde{\boldsymbol{\eta}}_{25}^{1024}$  and is only modest when the other initial conditions are used. Likewise, the norm  $\|\boldsymbol{\omega}(t)\|_{L^\infty}$  exhibits some weak growth only in the flow with the optimal initial condition  $\tilde{\boldsymbol{\eta}}_{25}^{1024}$  while it actually decreases for  $t \in [0, 25]$  when the initial conditions  $\boldsymbol{\eta}_{\text{TG}}$ ,  $\boldsymbol{\eta}_{\text{rand}}$  and  $\boldsymbol{\eta}_{\text{H}}$  are used.

## 4.2 Results for $T = 75$

We now move on to discuss solutions of Problem 2.2 on a longer time window with  $T = 75$  where the behavior of the “extreme” flows is qualitatively different from their behavior on the short time window discussed in Section 4.1. We begin our discussion by analyzing the effect of the initial guess  $\boldsymbol{\eta}_0$  on the local maximizers of Problem 2.2 obtained with the iterative algorithm (3.20). In figure 8(a) we show the dependence of the objective functional  $\Phi_{75}(\boldsymbol{\eta}^{(n)})$  on the iteration index  $n$  and figure 8(b) shows the energy spectra of the corresponding optimal initial conditions  $\tilde{\boldsymbol{\eta}}_{75}$ . We remark that, as an intermediate step, we first use the optimal initial condition  $\tilde{\boldsymbol{\eta}}_{25}^{128}$  as the initial guess to solve Problem 2.2 with  $T = 50$ , and then use its solution,  $\tilde{\boldsymbol{\eta}}_{50}^{128}$ , as the initial guess for  $T = 75$ . We see that, with the exception of the initial guess  $\boldsymbol{\eta}_{\text{K}}$ , computations performed with all other initial guesses lead to the same local maximizer (up to rotation and translation). As was the case when Problem 2.2 was solved with  $T = 25$ , computations using the initial guess  $\boldsymbol{\eta}_{\text{K}}$  lead to a much smaller maximum attained value of the objective functional since this initial condition is designed to promote a significant growth of various regularity indicators, such as  $\|\mathbf{u}(t)\|_{\dot{H}^3}$  and  $\|\boldsymbol{\omega}(t)\|_{L^\infty}$ , only on much longer time scales (Hou and Li, 2006).

As is evident from figure 8(b), computations carried out with the resolution  $128^3$  are under-resolved and now we consider the effect of refining the resolution on solutions of Problem 2.2 with  $T = 75$ . As we did in Section 4.1, we proceed by using the optimal initial condition  $\tilde{\boldsymbol{\eta}}_{75}^N$  as the initial guess in iteration (3.20) when solving Problem 2.2 with the resolution  $(2N)^3$ .

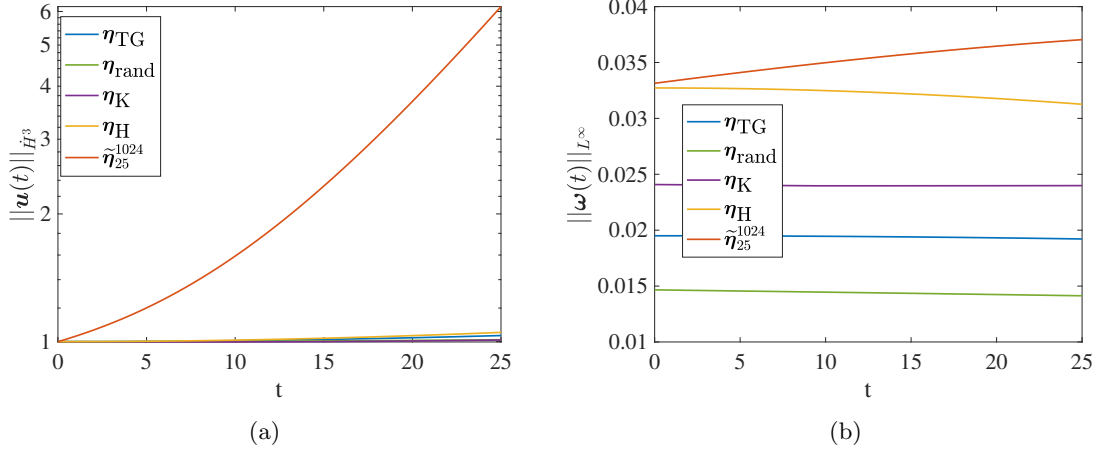


Figure 7: [Short time window,  $T = 25$ ] Dependence of the solution norms (a)  $\|\mathbf{u}(t)\|_{\dot{H}^3}$  and (b)  $\|\boldsymbol{\omega}(t)\|_{L^\infty}$  for  $t \in [0, 25]$  in Euler flows corresponding to different initial conditions and approximated using the resolution  $N^3 = 1024^3$ .

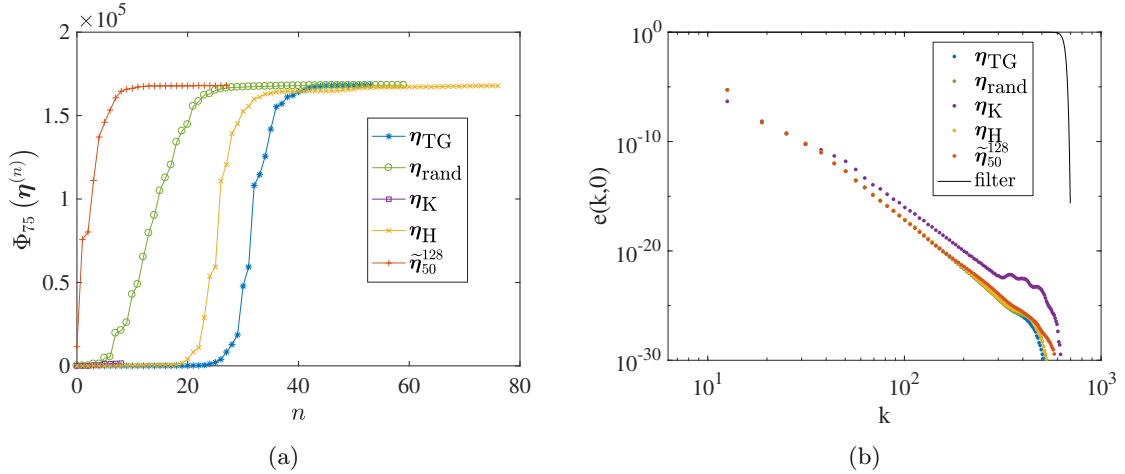


Figure 8: [Long time window,  $T = 75$ ] (a) Dependence of the objective functional  $\Phi_{75}(\boldsymbol{\eta}^{(n)})$  on the iteration index  $n$  and (b) energy spectra (3.37) of the optimal initial conditions  $\tilde{\boldsymbol{\eta}}_{75}$  corresponding to different initial guesses  $\boldsymbol{\eta}_{\text{TG}}$ ,  $\boldsymbol{\eta}_{\text{rand}}$ ,  $\boldsymbol{\eta}_{\text{K}}$  and  $\tilde{\boldsymbol{\eta}}_{25}$  used in iterations (3.20). In panel (b) the solid line represents the Gaussian filter we use (Hou and Li, 2007).

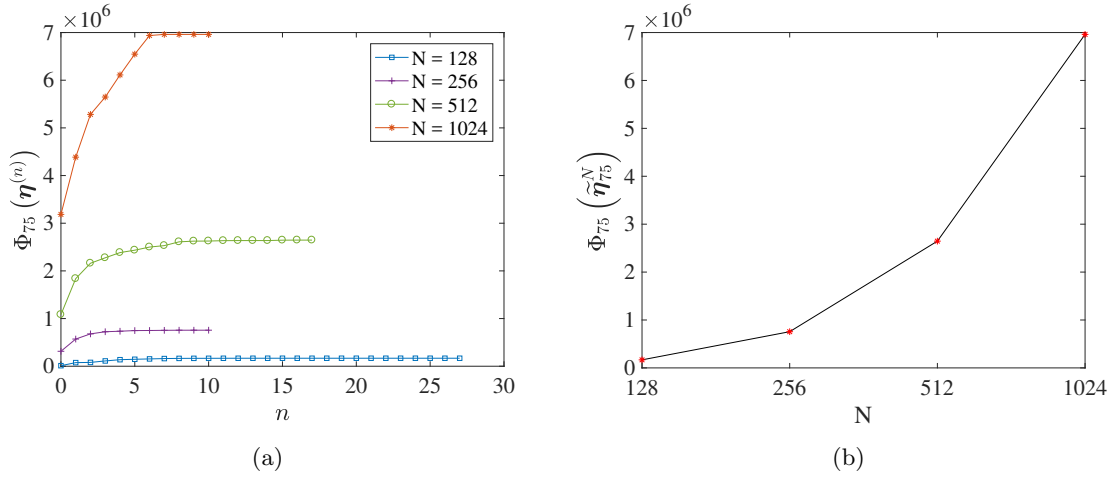


Figure 9: [Long time window,  $T = 75$ ] Dependence of (a) the objective functional  $\Phi_{75}^N(\eta^{(n)})$  on the iteration index  $n$  for different resolutions  $N^3$  and (b) of the corresponding maximum attained values  $\tilde{\Phi}_{75}^N$  of the objective functional on  $N$ .

The dependence of the objective functional  $\Phi_{75}^N(\eta^{(n)})$  on the iteration index  $n$  is presented for different resolutions in figure 9(a). Figure 9(b) shows that, unlike in the case with  $T = 25$ , cf. figure 4(b), the maximum attained values of the objective functional  $\tilde{\Phi}_{75}^N$  diverge as we refine the resolution with the difference  $\tilde{\Phi}_{75}^{2N} - \tilde{\Phi}_{75}^N$  increasing with  $N$ . As explained in Section 4, this indicates the possibility of a singularity formation at some  $t \in [0, 75]$ .

The energy spectra of the optimal initial conditions  $\tilde{\eta}_{75}^N$  and the corresponding terminal states  $\mathbf{u}^N(75; \tilde{\eta}_{75}^N)$  are shown in figures 10(a) and 10(b), respectively. Comparing these two figures, we observe that even though the initial conditions  $\tilde{\eta}_{75}^N$  are well-resolved for  $N = 512, 1024$ , the time evolutions computed with all resolutions become under-resolved at later times. In particular, for  $N = 1024$  this happens at  $t = T_0 := 51.25$  and is detected by the appearance of aliasing errors when the amplitudes of Fourier coefficients with wavenumbers  $|\mathbf{k}| > k_0$  become larger than  $10^{-30}$ . For lower resolutions, computations become under-resolved at earlier times. Once the numerical solution becomes under-resolved, its blow-up is prevented by the presence of the filter  $\hat{G}_j$  (cf. Section 3.3.1) which can be regarded as a form of dissipative regularization applied to the Euler system (1.1). Since the form of the filter depends on the resolution  $N$  (cf. figures 5 and 10), its regularizing effect vanishes when the resolution is refined, thereby allowing the computed solution to approach the singular trajectory as seen in figure 9(b).

The time evolution of the width  $\delta(t)$  of the analyticity strip and of the corresponding order  $n(t)$  of the singularity in optimal flows computed with  $N = 512, 1024$  is shown in figures 11(a) and 11(b), respectively. When determining these parameters by minimizing (3.40) we use  $k_> = k_0$ , i.e., the spectrum was fitted up to the maximum wavenumbers unaffected by aliasing. The fitting was also terminated whenever  $\delta(t) \leq 0$ . In figure 11(a) we see that, following an initial period of growth,  $\delta(t)$  starts to decrease when  $t > 40$  and this decrease follows a power-law behavior. According to the reliability conditions (4.3) indicated in figure 11(a), when  $N = 1024$ , we can trust the numerical computation up to time  $t = T_{\text{rel}} = 51.875$ ,

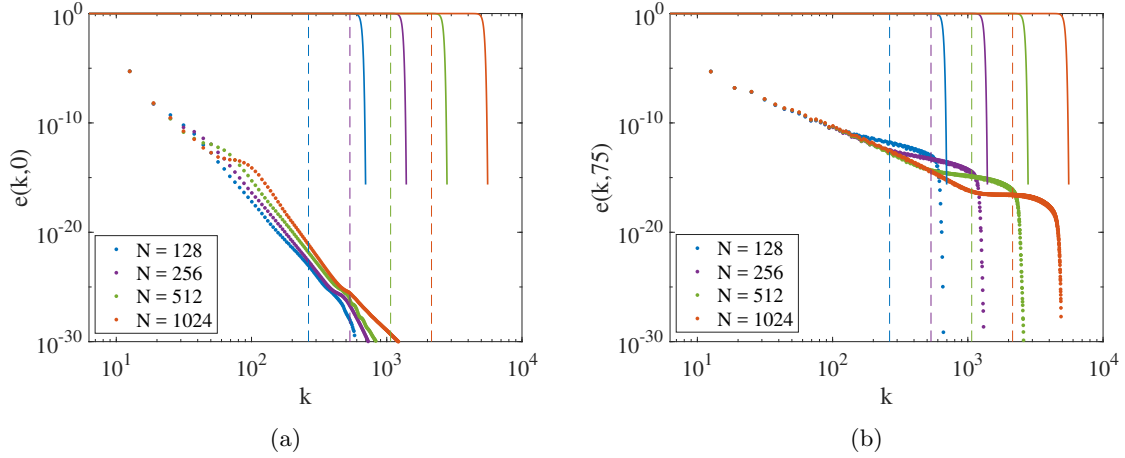


Figure 10: [Long time window,  $T = 75$ ] The energy spectra of (a) the optimal initial conditions  $\tilde{\boldsymbol{\eta}}_{75}^N$  and (b) of the corresponding terminal states  $\mathbf{u}^N(75; \tilde{\boldsymbol{\eta}}_{75}^N)$  obtained for different resolutions  $N^3$ . The solid lines represent the Gaussian filters we use (Hou and Li, 2007) whereas the dashed lines mark the threshold wavenumber  $k_0$  above which aliasing errors occur.

which is close to, but slightly longer, than the time  $T_0$  when aliasing errors appear. This is reasonable as there is a delay in the effect of aliasing errors on the part of the spectrum which determines the width of the analyticity strip.

The time evolution of  $\|\mathbf{u}(t)\|_{\dot{H}^3}$  and  $\|\boldsymbol{\omega}(t)\|_{L^\infty}$  in the flows corresponding to different initial conditions is shown in figures 12(a) and 12(b), respectively. As was the case in Section 4.1, a significant growth of these norms is evident only in the flows corresponding to the optimal initial condition  $\tilde{\boldsymbol{\eta}}_{75}^{1024}$ , whereas  $\|\boldsymbol{\omega}(t)\|_{L^\infty}$  actually decreases on  $[0, 75]$  for solutions with the initial conditions  $\boldsymbol{\eta}_{\text{TG}}$ ,  $\boldsymbol{\eta}_{\text{rand}}$  and  $\boldsymbol{\eta}_{\text{H}}$ . As regards the time evolution of the latter quantity, Bustamante and Brachet (2012, Corollaries 10 and 11) used the BKM criterion (1.2) to obtain a condition (whose details are omitted for brevity) which must be satisfied by the exponent  $\Gamma(t) > 0$  in an ansatz describing the evolution of the width of the analyticity strip under the assumption of finite-time blow-up, namely  $\delta(t) = C(t)(T^* - t)^{\Gamma(t)}$ , and the corresponding evolution of the order of singularity  $n(t)$ . The flow evolution corresponding to the optimal initial data  $\tilde{\boldsymbol{\eta}}_{75}^{1024}$  satisfies this condition, indicating that this evolution is consistent with a possible singularity formation in finite time despite modest growth of the norm  $\|\boldsymbol{\omega}(t)\|_{L^\infty}$  evident in figure 12(b).

In order to shed light on whether the growth of the norm  $\|\mathbf{u}(t)\|_{\dot{H}^3}$  observed in figure 12(a) corresponding to the optimal initial conditions  $\tilde{\boldsymbol{\eta}}_{75}^N$  may indicate a singularity formation at some time  $t \in [0, 75]$ , we further analyze the growth rate of  $\|\mathbf{u}(t)\|_{\dot{H}^3}$ . We assume that the evolution of this norm is described by the relation

$$\frac{d\|\mathbf{u}(t)\|_{\dot{H}^3}}{dt} = C(t)\|\mathbf{u}(t)\|_{\dot{H}^3}^{\alpha(t)}, \quad (4.4)$$

which is motivated by the structure of rigorous a priori estimates for the rate of growth of Sobolev norms of solutions to the Navier-Stokes system (Doering and Gibbon, 1995; Lu and Doering, 2008; Ayala and Protas, 2017). We note that if the exponent  $\alpha(t)$  in (4.4) remains

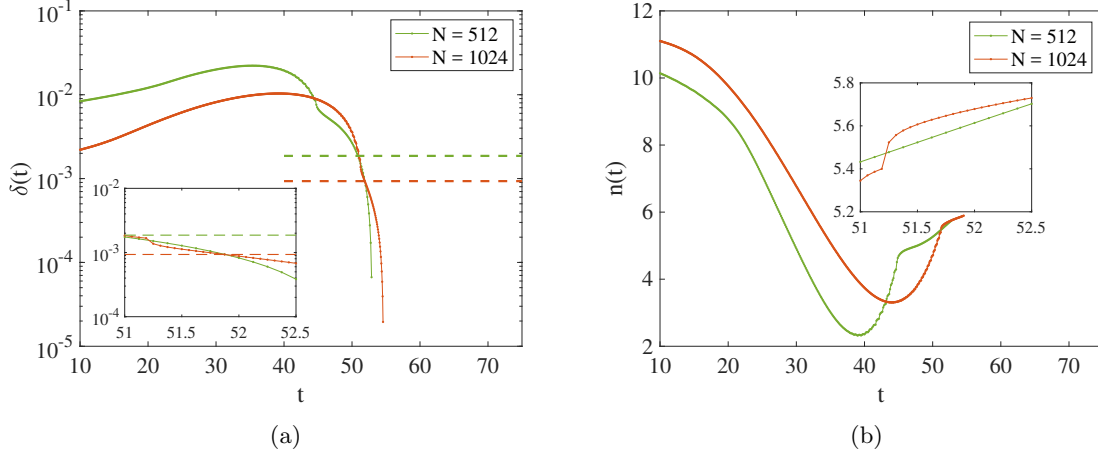


Figure 11: [Long time window,  $T = 75$ ] Dependence of (a) the width  $\delta(t)$  of the analyticity strip and (b) the corresponding order  $n(t)$  of the singularity, cf. (3.39), on time  $t \in [0, 75]$  in the extreme flows computed with resolutions  $N^3 = 512^3, 1024^3$ . In (a) the horizontal lines represent the reliability condition (4.3) corresponding to different resolutions.

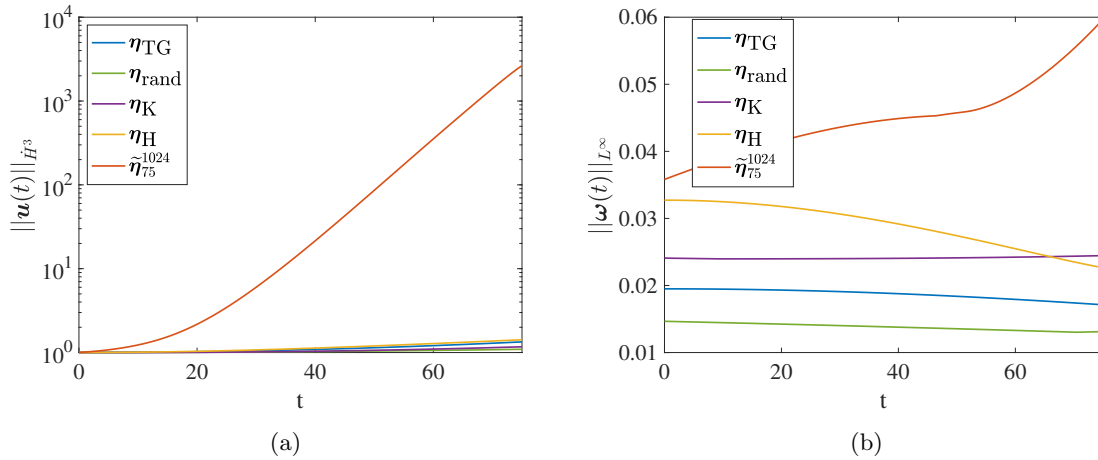


Figure 12: [Long time window,  $T = 75$ ] Dependence of the solution norms (a)  $\|\mathbf{u}(t)\|_{\dot{H}^3}$  and (b)  $\|\boldsymbol{\omega}(t)\|_{L^\infty}$  for  $t \in [0, 75]$  in Euler flows corresponding to different initial conditions and approximated using the resolution  $N^3 = 1024^3$ .



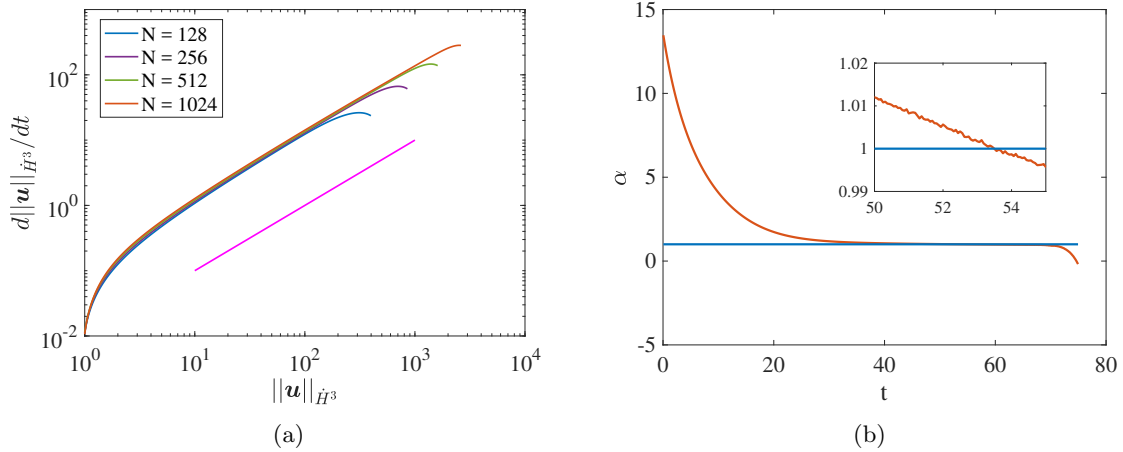


Figure 13: [Long time window,  $T = 75$ ] (a) Dependence of  $(d/dt)\|\mathbf{u}(t)\|_{\dot{H}^3}$  on  $\|\mathbf{u}(t)\|_{\dot{H}^3}$  in Euler flows with the optimal initial conditions  $\tilde{\boldsymbol{\eta}}_{75}^N$  for  $t \in [0, 75]$  and different resolutions  $N^3$  and (b) the corresponding exponent  $\alpha(t)$  in (4.4) for  $t \in [0, 75]$  with  $N = 1024$ . The straight lines in both panels represent  $\alpha = 1$ .

larger than 1 over a sufficiently long time with the prefactor  $C(t)$  bounded away from zero, then there will be a finite-time blow-up of the norm  $\|\mathbf{u}(t)\|_{\dot{H}^3}$ , and thus formation of a singularity in the corresponding Euler flow, cf. Theorem 1.1. To obtain further insights about these quantities, in figure 13(a) we plot  $(d/dt)\|\mathbf{u}(t)\|_{\dot{H}^3}$  versus  $\|\mathbf{u}(t)\|_{\dot{H}^3}$  with  $t \in [0, 75]$  using log-log scaling for the optimal flows computed with different resolutions, such that the exponent  $\alpha(t)$  can be inferred from the slope of the tangent to the curves at  $\|\mathbf{u}(t)\|_{\dot{H}^3}$ . The evolution of the exponent  $\alpha(t)$  determined by a local fitting procedure applied to ansatz (4.4) with time  $t \in [0, 75]$  is shown for  $N = 1024$  in figure 13(b), where a decreasing trend is evident and we have  $\alpha(t) > 1$  for  $t \in [0, 53.495]$  while the computation becomes under-resolved at  $t \approx 51.25$ . As regards the prefactor  $C(t)$  in (4.4), it reveals a slow growth with time  $t$  (and with  $\|\mathbf{u}(t)\|_{\dot{H}^3}$ ) which is well approximated by the expression  $C(t) = 0.0568 (\ln \|\mathbf{u}(t)\|_{\dot{H}^3})^{0.5742}$  with parameters determined via a least-squares fit. We thus conclude that the time evolution of the norm  $\|\mathbf{u}(t)\|_{\dot{H}^3}$  in the flow with the optimal initial condition  $\tilde{\boldsymbol{\eta}}_{75}^{1024}$  remains consistent with the singularity formation as long as the computation remains well-resolved.

Finally, we analyze the physical-space structure of the extreme flow, beginning with the vorticity field of the optimal initial condition  $\tilde{\boldsymbol{\omega}}_{75}^{1024} = [\omega_1, \omega_2, \omega_3] = \nabla \times \tilde{\boldsymbol{\eta}}_{75}^{1024}$ . In figure 14, we show the three components of  $\tilde{\boldsymbol{\omega}}_{75}^{1024}$  and observe that the optimal initial condition has the form of three perpendicular pairs of distorted anti-parallel vortex tubes. If we define the component-wise enstrophy as  $\mathcal{E}_i := \frac{1}{2} \int_{\mathbb{T}^3} \omega_i^2(\mathbf{x}) d\mathbf{x}$ ,  $i = 1, 2, 3$ , then we have  $\mathcal{E}_1 = 6.34 \times 10^{-5} \approx \mathcal{E}_2 = 6.35 \times 10^{-5} < \mathcal{E}_3 = 8.03 \times 10^{-5}$ , which is a signature of the symmetry of the flow with respect to the plane  $x_1 = x_2$ . The helicity of the optimal flow defined as  $\mathcal{H}(t) = \int_{\mathbb{T}^3} h(\mathbf{x}, t) d\mathbf{x}$ , where  $h(\mathbf{x}, t) := \mathbf{u}(\mathbf{x}, t) \cdot \boldsymbol{\omega}(\mathbf{x}, t)$  is the helicity density, vanishes (it is an invariant of the evolution). The helicity density  $h(\mathbf{x}, 0)$  of the optimal initial condition  $\tilde{\boldsymbol{\eta}}_{75}^{1024}$  is shown in figure 14(d) revealing that the vanishing of the helicity  $\mathcal{H}(t)$ ,  $t \geq 0$ , is a consequence of the aforementioned symmetry. In fact, this initial condition possesses a similar physical-space structure as the one

found in Kang et al. (2020), where the authors searched for singularities in Navier-Stokes flows by maximizing the total enstrophy at a prescribed final time. While, unlike here, no evidence for singularity formation was revealed in that earlier study.

Next, in figure 15(a), we analyze the optimal initial condition  $\tilde{\boldsymbol{\eta}}_{75}^{1024}$  in more detail with the corresponding terminal state  $\mathbf{u}^{1024}$  ( $75; \tilde{\boldsymbol{\eta}}_{75}^{1024}$ ) shown in figure 15(b). In both figures we show the isosurfaces of  $|\boldsymbol{\omega}|$  and  $\log_{10} (||D|^3\mathbf{u}|)$  together with selected streamlines passing through a small neighborhood of the origin (see also Movie 1 available in Supplementary Material). We observe that throughout its evolution the optimal flow has the form of two jets colliding head-on with the vorticity concentrating into two strongly flattened vortex rings as time goes on. The region with large values of  $\log_{10} (||D|^3\mathbf{u}|)$ , which is the quantity that matters in our objective functional (2.7), evolves into a flat disc located in the middle of the two rings. The vorticity field at the final time  $t = 75$  has three symmetry planes:  $x_1 = x_2$ ,  $x_1 = x_3$  and  $x_2 = x_3$ , in addition to discrete rotation symmetries with respect to the body diagonal passing through the center of the two rings. Without loss of generality, we focus our discussion on the symmetry plane  $x_1 = x_2$ , and in figures 16(a) and 16(b) we visualize the vorticity component  $\omega^\perp := \boldsymbol{\omega} \cdot \mathbf{n}$  normal to that plane ( $\mathbf{n} = \left[-\frac{1}{\sqrt{2}}, \frac{1}{\sqrt{2}}, 0\right]^T$  is the unit vector normal to the symmetry plane), at  $t = 0$  and  $t = 75$  (see also Movie 2 available in Supplementary Material). The streamline pattern in figure 15 (b) indicates that as  $t$  approaches 75, the flow in the two jets colliding near the origin sharply transitions towards a radial outflow through the gap between the two vortex rings. At the same time, this gap becomes very narrow, which results in a sharp transition between the regions of the symmetry plane characterized by opposite signs of the normal vorticity  $\omega^\perp$ , cf. figure 16(b). This appears to be the mechanism responsible for the possible singularity formation in the extreme flow considered here.

## 5 Discussion and conclusions

In this paper, we study the problem concerning the possibility of spontaneous formation of singularities in solutions of the 3D Euler equations (1.1) on a periodic domain. Based on the local well-posedness results by Kato (1972) stated in Theorem 1.1, we formulate a PDE-constrained optimization problem to search for initial conditions  $\boldsymbol{\eta}$  with unit  $\dot{H}^3$  seminorm such that the corresponding optimal solution achieves a maximum  $\dot{H}^3$  seminorm at a prescribed time  $T$ . Since we focus on smooth (real-analytic) initial data, the optimization problem is formulated in a suitable Gevrey space (2.4). It is then solved in the “optimize-then-discretize” setting using a state-of-the-art Riemannian conjugate gradient method (3.20) where the search direction at every iteration depends on the gradient of the objective functional at the current iteration as well as on the previous search direction; the former is obtained by solving the adjoint system (3.8) backward in time. The required regularity of the gradient is ensured by the use of the Riesz representation theorem, cf. (3.4). An analogous approach has been successfully used to solve PDE-constrained optimization problems formulated to elucidate extreme behaviors in 1D Burgers (Ayala and Protas, 2011) and 3D Navier-Stokes flows (Kang et al., 2020; Kang and Protas, 2021).

Problem 2.2 is non-convex and we have found evidence for the presence of nonunique local maximizers corresponding to different initial guesses listed in § 3.3.2. However, iterations performed with most initial guesses were found to converge to the same (up to rotation and translation) local maximizer, with the exception of the initial guess  $\boldsymbol{\eta}_K$ , which was designed

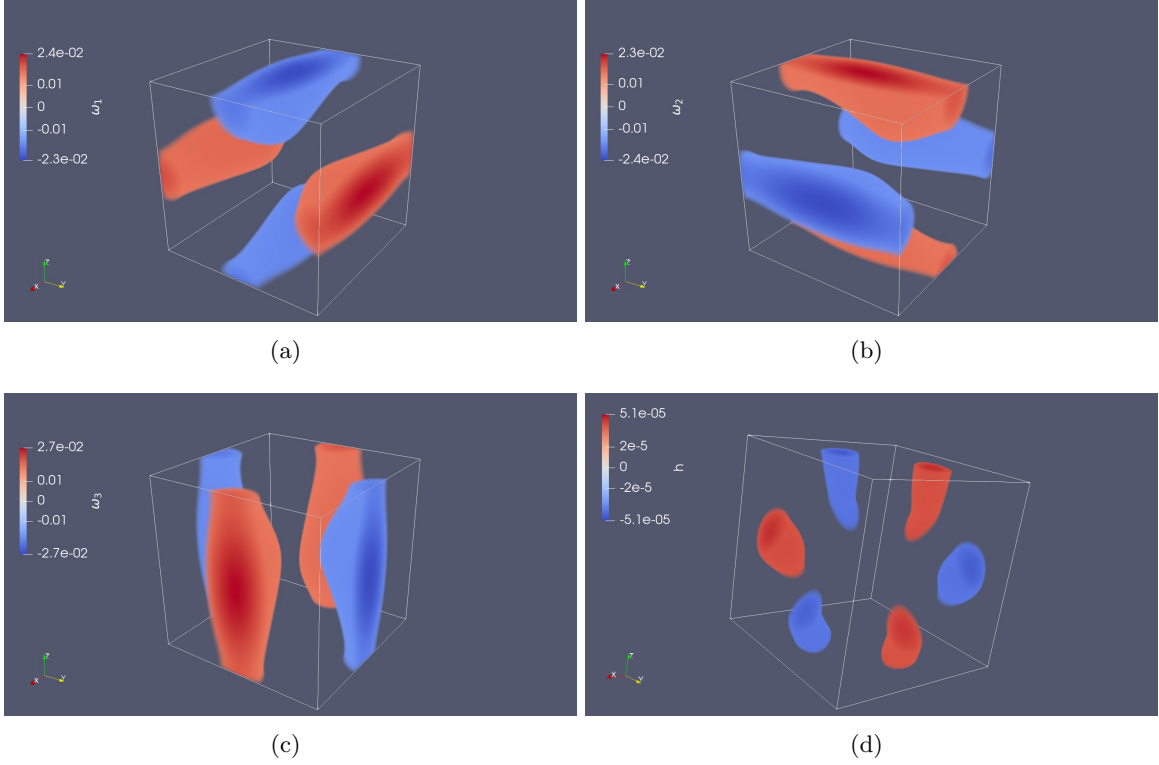


Figure 14: [Long time window,  $T = 75$ ] Isosurfaces of the components (a)  $\omega_1$ , (b)  $\omega_2$  and (c)  $\omega_3$  of the vorticity field and of (d) the helicity density  $h(\mathbf{x}, 0)$  corresponding to the optimal initial condition  $\tilde{\boldsymbol{\eta}}_{75}^{1024}$ .

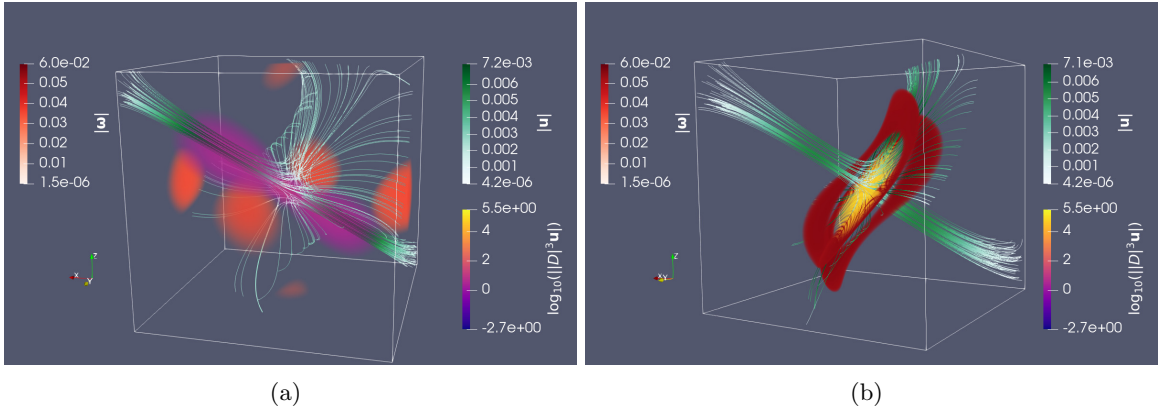


Figure 15: [Long time window,  $T = 75$ ] Isosurfaces of  $|\boldsymbol{\omega}|$  and  $\log_{10}(|D^3\mathbf{u}|)$  in (a) the optimal initial condition  $\tilde{\boldsymbol{\eta}}_{75}^{1024}$  and (b) the corresponding terminal state  $\mathbf{u}^{1024}(75; \tilde{\boldsymbol{\eta}}_{75}^{1024})$  together with selected streamlines. The same color ranges are used in both panels. An animated version of these figures (without streamlines) showing the time evolution for  $t \in [0, 75]$  is available as Movie 1.

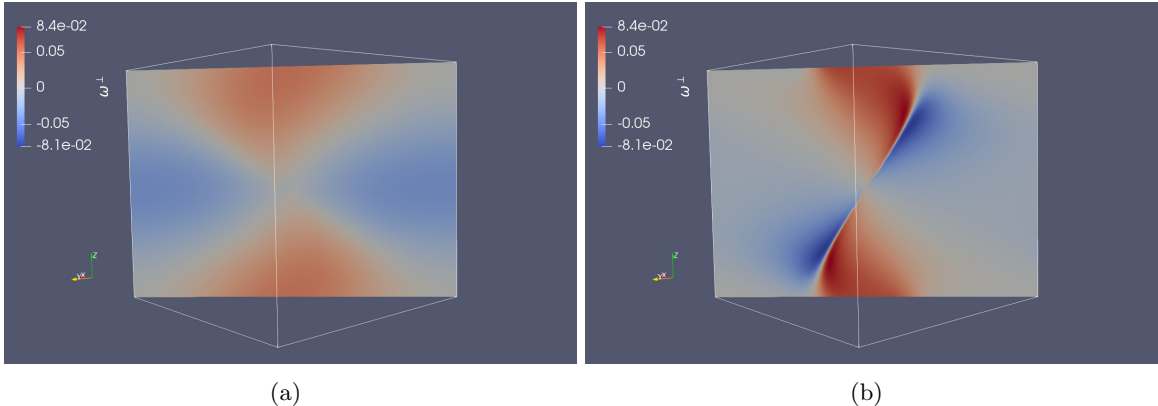


Figure 16: [Long time window,  $T = 75$ ] The vorticity component  $\omega^\perp$  normal to the symmetry plane  $x_1 = x_2$  in (a) the optimal initial condition  $\tilde{\eta}_{75}^{1024}$  and (b) the corresponding terminal state  $\mathbf{u}^{1024}(75; \tilde{\eta}_{75}^{1024})$ . The same color range is used in both panels. An animated version of these figures showing the time evolution for  $t \in [0, 75]$  is available as Movie 2.

to produce significant growth of various regularity indicators at times much longer than the intervals  $[0, T]$  considered in this study.

We adopt an indirect approach to determine whether a singularity may occur within the time interval  $[0, T]$  based on sequential refinements of the numerical resolution. Specifically, we solve Problem 2.2 with  $T = 25$  and  $T = 75$  using spatial resolutions increasing from  $128^3$  to  $1024^3$ . For  $T = 25$ , we observe that the maximum attained values of  $\|\mathbf{u}^N(75; \tilde{\eta}_{75}^N)\|_{\dot{H}^3}$  converge to a finite limit for the optimal solutions obtained with increasing resolutions, which indicates that the Euler system (1.1) is well-posed on  $[0, 25]$ . However, for  $T = 75$ , the maximum values of  $\|\mathbf{u}^N(75; \tilde{\eta}_{75}^N)\|_{\dot{H}^3}$  attained in the optimal solutions diverge upon resolution refinement, which suggests a possible formation of singularity for some  $t \in [0, 75]$ . As shown in figure 13, the growth of the norm  $\|\mathbf{u}(t)\|_{\dot{H}^3}$  in the flows corresponding to the optimal initial condition obtained for  $T = 75$  using the highest numerical resolution proceeds at a rate consistent with a finite-time blow-up as long as the solution remains well-resolved, although this rate slows down with time. With the limited numerical resolution we could use, it is impossible to conclude whether this depletion of growth rate would eventually prevent a singularity from appearing in a finite time. We add that the largest resolution we used ( $1024^3$ ) is smaller than the largest resolutions available to-date in simulations of the Navier-Stokes and the Euler systems. However, we emphasize that in the present study we solve a family of optimization problems which are much more costly to solve than simply computing the evolution of the solution on the same time interval. In fact, solution of Problem 2.2 typically requires  $\mathcal{O}(100)$  solutions of the Euler system (1.1) and  $\mathcal{O}(10)$  solutions of the adjoint system (3.8).

We add that under-resolved computations of Euler flows lead to “thermalization” of solutions, a process where after a sufficiently long time the kinetic energy is equidistributed among the finite number of Fourier modes used in the computation. Thermalization is related to the appearance of the so-called “tygers” and inevitably occurs when using numerical methods based on Galerkin truncation to compute the time evolution of inviscid systems, such as 1D Burgers equation (Rampf et al., 2022) and 3D incompressible Euler equations (Murugan and

Ray, 2022).

Figures 7 and 12 show that, as compared to flows obtained with different initial guesses, the optimal flows demonstrate a more significant growth in both  $\|\mathbf{u}(t; \tilde{\boldsymbol{\eta}})\|_{\dot{H}^3}$  and  $\|\boldsymbol{\omega}(t; \tilde{\boldsymbol{\eta}})\|_{L^\infty}$  throughout the optimization time windows  $[0, T]$  with  $T = 25$  and  $T = 75$ . We further notice that the growth of the norm  $\|\boldsymbol{\omega}(t)\|_{L^\infty}$  in the extreme flows obtained by solving Problem 2.2 with  $T = 75$  is weaker than the growth of the norm  $\|\mathbf{u}(t)\|_{\dot{H}^3}$  in the same flow, cf. figures 12(a) and 12(b). However, estimate (1.4) shows that an unbounded growth of the latter norm implies such a growth for the former norm as well, and the doubly-exponential structure of the upper bound in this estimate explains why in a blow-up scenario the growth of  $\|\boldsymbol{\omega}(t)\|_{L^\infty}$  may be weaker than that of  $\|\mathbf{u}(t)\|_{\dot{H}^3}$ . As regards the behavior of the width  $\delta(t)$  of the analyticity strip in these flows, we note that the decay rate of this quantity accelerates and becomes faster than exponential around the time when computations become under-resolved.

In regard to the structure of the extreme flows in the physical space, it is interesting to see in figure 15(b) that some key features of these flows are close to being axisymmetric, to the extent that this may be possible for a flow evolving on a 3D periodic domain. More specifically, the region where the largest values of  $\|D^3\mathbf{u}\|$  are concentrated has the form of a circular disc embedded between the two colliding vortex rings, which becomes more irregular further away from the axis of symmetry. The center of this disk, located on the symmetry plane of the extreme flows, is a stagnation point; in this sense, the extreme flows are similar to the infinite-energy solutions of the Euler system constructed by Gibbon et al. (1999), which are known to exhibit finite-time singularities (Mulungye et al., 2016). We emphasize that the extreme flows we found here are fairly robust in the sense that they have been found consistently using several different initial guesses in (3.20), albeit not with all initial guesses we used. We add that a head-on collision of two vortex rings has served as a classical paradigm in recent experimental and numerical studies of turbulence generation (McKeown et al., 2018; Lim and Nickels, 1992; McKeown et al., 2020). At high Reynolds numbers, these two vortex rings break down into smaller antiparallel secondary and tertiary filaments, eventually forming a turbulent cloud due to the elliptic instability (McKeown et al., 2020).

As concerns future work, the properties of the optimal flows found in the present study suggest looking for extreme behaviors among initial conditions constrained by some symmetries, such as axial and/or reflection symmetries, as was pursued by Luo and Hou (2014a,b); Hou (2022). In addition, given that spectral methods have a limited ability to resolve localized small-scale features of potentially singular flows, further progress will likely require the use of adaptive discretization techniques.

## Acknowledgements

The authors wish to express thanks to Marc Brachet, Miguel Bustamante, John Gibbon, Robert Kerr, Adam Larios and Thomas Y. Hou for enlightening and enjoyable discussions. The authors also acknowledge the support through an NSERC (Canada) Discovery Grant. Computational resources were provided by Digital Research Alliance of Canada under its Resource Allocation Competition.

## References

- P.-A. Absil, R. Mahony, and R. Sepulchre. *Optimization Algorithms on Matrix Manifolds*. Princeton University Press, 2008.
- R. A. Adams and J. F. Fournier. *Sobolev Spaces*. Elsevier, 2005.
- D. Ayala. *Extreme Vortex States and Singularity Formation in Incompressible Flows*. PhD thesis, McMaster University, 2014. available at <http://hdl.handle.net/11375/15453>.
- D. Ayala and B. Protas. On maximum enstrophy growth in a hydrodynamic system. *Physica D*, 240:1553–1563, 2011.
- D. Ayala and B. Protas. Maximum palinstrophy growth in 2D incompressible flows. *Journal of Fluid Mechanics*, 742:340–367, 2014.
- D. Ayala and B. Protas. Extreme vortex states and the growth of enstrophy in 3D incompressible flows. *Journal of Fluid Mechanics*, 818:772–806, 2017.
- Claude Bardos and S Benachour. Domaine d’analyticit  des solutions de l’ quation d’Euler dans un ouvert de  $R^n$ . *Annali della Scuola Normale Superiore di Pisa-Classe di Scienze*, 4(4): 647–687, 1977.
- J. T. Beale, T. Kato, and A. Majda. Remarks on the breakdown of smooth solutions for the 3-D Euler equations. *Comm. Math. Phys.*, 94(1):61–66, 1984. URL <http://projecteuclid.org/euclid.cmp/1103941230>.
- M. E. Brachet. Direct simulation of three-dimensional turbulence in the Taylor-Green vortex. *Fluid Dynamics Research*, 8:1–8, 1991.
- M. E. Brachet, D. I. Meiron, S. A. Orszag, B. G. Nickel, R. H. Morf, and U. Frisch. Small-scale structure of the Taylor-Green vortex. *Journal of Fluid Mechanics*, 130:411–452, 1983.
- M. D. Bustamante and M. Brachet. Interplay between the Beale-Kato-Majda theorem and the analyticity-strip method to investigate numerically the incompressible Euler singularity problem. *Phys. Rev. E*, 86:066302, 2012.
- M. D. Bustamante and R. M. Kerr. 3D Euler about a 2D symmetry plane. *Physica D*, 237: 1912–1920, 2008.
- Ciro S. Campolina and Alexei A. Mailybaev. Chaotic Blowup in the 3D Incompressible Euler Equations on a Logarithmic Lattice. *Phys. Rev. Lett.*, 121:064501, Aug 2018. doi: 10.1103/PhysRevLett.121.064501. URL <https://link.aps.org/doi/10.1103/PhysRevLett.121.064501>.
- George F. Carrier, Max Krook, and Carl E. Pearson. *Functions of a Complex Variable: Theory and Technique*. Society for Industrial and Applied Mathematics, 2005. doi: 10.1137/1.9780898719116. URL <https://epubs.siam.org/doi/abs/10.1137/1.9780898719116>.
- Dongho Chae. On the Well-Posedness of the Euler Equations in the Besov and the Triebel-Lizorkin Spaces. *Tosio Kato’s Method and Principle for Evolution Equations in Mathematical Physics*, pages 42–57, 2001.

- Jiajie Chen and Thomas Y Hou. Stable nearly self-similar blowup of the 2D Boussinesq and 3D Euler equations with smooth data. *arXiv preprint arXiv:2210.07191*, 2022.
- Thomas Chen and Nataša Pavlović. A lower bound on blowup rates for the 3D incompressible Euler equation and a single exponential Beale-Kato-Majda type estimate. *Commun. Math. Phys.*, 314(1):265–280, 2012.
- C. Cichowlas and M. E. Brachet. Evolution of complex singularities in Kida-Pelz and Taylor-Green inviscid flows. *Fluid Dynamics Research*, 36:239–248, 2005.
- Peter Constantin, Weinan E, and Edriss S. Titi. Onsager’s conjecture on the energy conservation for solutions of Euler’s equation. *Communications in Mathematical Physics*, 165(1): 207 – 209, 1994. doi: cmp/1104271041. URL <https://doi.org/>.
- Peter Constantin, Charles Fefferman, and Andrew J Majda. Geometric constraints on potentially singular solutions for the 3-D Euler equations. *Communications in Partial Differential Equations*, 21(3-4), 1996.
- Ionut Danaïla and Bartosz Protas. Computation of Ground States of the Gross–Pitaevskii Functional via Riemannian Optimization. *SIAM Journal on Scientific Computing*, 39(6):B1102–B1129, 2017. doi: 10.1137/17M1121974. URL <https://doi.org/10.1137/17M1121974>.
- Camillo De Lellis and László Székelyhidi Jr. On turbulence and geometry: from Nash to Onsager. *Notices Amer. Math. Soc.*, 66(5):677–685, 2019. URL <http://cvgmt.sns.it/paper/4181/>. cvgmt preprint.
- Jian Deng, Thomas Y Hou, and Xinwei Yu. Geometric properties and non-blowup of 3D incompressible Euler flow. *Communications in Partial Difference Equations*, 30(1-2):225–243, 2005.
- C. R. Doering. The 3D Navier-Stokes problem. *Annual Review of Fluid Mechanics*, 41:109–128, 2009.
- C. R. Doering and J. D. Gibbon. *Applied Analysis of the Navier-Stokes Equations*. Cambridge University Press, 1995.
- Tarek M Elgindi. Finite-time singularity formation for  $C^{1,\alpha}$  solutions to the incompressible Euler equations on  $\mathbb{R}^3$ . *Annals of Mathematics*, 194(3):647–727, 2021.
- Tarek M. Elgindi and In-Jee Jeong. Finite-Time Singularity Formation for Strong Solutions to the Axi-symmetric 3D Euler Equations. *Annals of PDE*, 5(2):16, Oct 2019. ISSN 2199-2576. doi: 10.1007/s40818-019-0071-6. URL <https://doi.org/10.1007/s40818-019-0071-6>.
- C. L. Fefferman. Existence and smoothness of the Navier-Stokes equation. available at <http://www.claymath.org/sites/default/files/navierstokes.pdf>, 2000. Clay Millennium Prize Problem Description.
- Niklas Fehn, Martin Kronbichler, Peter Munch, and Wolfgang A Wall. Numerical evidence of anomalous energy dissipation in incompressible Euler flows: towards grid-converged results for the inviscid Taylor–Green problem. *Journal of Fluid Mechanics*, 932, 2022.

- Matteo Frigo and Steven G. Johnson. *FFTW User's Manual*. Massachusetts Institute of Technology, 2003.
- J. D. Gibbon, M. Bustamante, and R. M. Kerr. The three-dimensional Euler equations: singular or non-singular? *Nonlinearity*, 21:123–129, 2008.
- J.D. Gibbon. Dynamics of Scaled Norms of Vorticity for the Three-dimensional Navier-Stokes and Euler Equations. *Procedia IUTAM*, 7:39–48, 2013. ISSN 2210-9838. doi: <https://doi.org/10.1016/j.piutam.2013.03.006>. URL <https://www.sciencedirect.com/science/article/pii/S2210983813000308>. IUTAM Symposium on Topological Fluid Dynamics: Theory and Applications.
- J.D. Gibbon, A.S. Fokas, and C.R. Doering. Dynamically stretched vortices as solutions of the 3d navier-stokes equations. *Physica D: Nonlinear Phenomena*, 132(4):497–510, 1999. ISSN 0167-2789. doi: [https://doi.org/10.1016/S0167-2789\(99\)00067-6](https://doi.org/10.1016/S0167-2789(99)00067-6). URL <https://www.sciencedirect.com/science/article/pii/S0167278999000676>.
- T. Grafke, H. Homann, J. Dreher, and R. Grauer. Numerical simulations of possible finite-time singularities in the incompressible Euler equations: comparison of numerical methods. *Physica D*, 237:1932–1936, 2008.
- M. D. Gunzburger. *Perspectives in Flow Control and Optimization*. SIAM, 2003.
- Hui Guo, Xueting Liang, and Yang Yang. Provable convergence of blow-up time of numerical approximations for a class of convection-diffusion equations. *Journal of Computational Physics*, 466:111421, 2022.
- T. Y. Hou. Blow-up or no blow-up? a unified computational and analytic approach to 3D incompressible Euler and Navier-Stokes equations. *Acta Numerica*, pages 277–346, 2009.
- T. Y. Hou and R. Li. Computing nearly singular solutions using pseudo-spectral methods. *Journal of Computational Physics*, 226:379–397, 2007.
- Thomas Y Hou. Potential singularity of the 3D Euler equations in the interior domain. *Foundations of Computational Mathematics*, pages 1–47, 2022.
- Thomas Y Hou and Ruo Li. Dynamic depletion of vortex stretching and non-blowup of the 3-D incompressible Euler equations. *Journal of Nonlinear Science*, 16(6):639–664, 2006.
- D. Kang and B. Protas. Searching for Singularities in Navier-Stokes Flows Based on the Ladyzhenskaya-Prodi-Serrin Conditions. arXiv:2110.06130, 2021.
- Di Kang, Dongfang Yun, and Bartosz Protas. Maximum amplification of enstrophy in three-dimensional Navier-Stokes flows. *Journal of Fluid Mechanics*, 893:A22, 2020. doi: 10.1017/jfm.2020.204.
- Tosio Kato. Nonstationary flows of viscous and ideal fluids in  $\mathbb{R}^3$ . *Journal of functional Analysis*, 9(3):296–305, 1972.
- R. M. Kerr. Evidence for a singularity of the three-dimensional, incompressible Euler equations. *Phys. Fluids A*, 5:1725–1746, 1993.



- Robert M. Kerr. Swirling, turbulent vortex rings formed from a chain reaction of reconnection events. *Physics of Fluids*, 25:065101, 2013.
- Hideo Kozono and Yasushi Taniuchi. Limiting Case of the Sobolev Inequality in BMO, with Application to the Euler Equations. *Communications in Mathematical Physics*, 214(1):191–200, 2000.
- Igor Kukavica and Vlad Vicol. On the radius of analyticity of solutions to the three-dimensional Euler equations. *Proceedings of the American Mathematical Society*, 137(2):669–677, 2009.
- Adam Larios, Mark R. Petersen, Edriss S. Titi, and Beth Wingate. A computational investigation of the finite-time blow-up of the 3d incompressible euler equations based on the voigt regularization. *Theoretical and Computational Fluid Dynamics*, 32(1):23–34, Feb 2018. ISSN 1432-2250. doi: 10.1007/s00162-017-0434-0. URL <https://doi.org/10.1007/s00162-017-0434-0>.
- Leon Lichtenstein. Über einige existenzprobleme der hydrodynamik homogener, unzusammen-drückbarer, reibungsloser flüssigkeiten und die helmholtzschen wirbelsätze. *Mathematische Zeitschrift*, 23(1):89–154, Dec 1925. ISSN 1432-1823. doi: 10.1007/BF01506223. URL <https://doi.org/10.1007/BF01506223>.
- T.T. Lim and T.B. Nickels. Instability and reconnection in the head-on collision of two vortex rings. *Nature*, 357(6375):225–227, 1992.
- L. Lu and C. R. Doering. Limits on enstrophy growth for solutions of the three-dimensional Navier–Stokes equations. *Indiana University Mathematics Journal*, 57:2693–2727, 2008.
- D. Luenberger. *Optimization by Vector Space Methods*. John Wiley and Sons, 1969.
- G. Luo and T. Y. Hou. Potentially Singular Solutions of the 3D Axisymmetric Euler Equations. *Proceedings of the National Academy of Sciences*, 111(36):12968–12973, 2014a.
- G. Luo and T. Y. Hou. Toward the Finite-Time Blowup of the 3D Incompressible Euler Equations: a Numerical Investigation. *SIAM: Multiscale Modeling and Simulation*, 12(4):1722–1776, 2014b.
- A. J. Majda and A. L. Bertozzi. *Vorticity and Incompressible Flow*. Cambridge University Press, 2002.
- T. Matsumoto, J. Bec, and U. Frisch. Complex-space singularities of 2D Euler flow in lagrangian coordinates. *Physica D*, 237:1951–1955, 2008.
- Ryan McKeown, Rodolfo Ostilla-Mónico, Alain Pumir, Michael P Brenner, and Shmuel M Rubinstein. Cascade leading to the emergence of small structures in vortex ring collisions. *Physical Review Fluids*, 3(12):124702, 2018.
- Ryan McKeown, Rodolfo Ostilla-Mónico, Alain Pumir, Michael P Brenner, and Shmuel M Rubinstein. Turbulence generation through an iterative cascade of the elliptical instability. *Science advances*, 6(9):eaaz2717, 2020.

- Rachel M. Mulungye, Dan Lucas, and Miguel D. Bustamante. Atypical late-time singular regimes accurately diagnosed in stagnation-point-type solutions of 3d euler flows. *Journal of Fluid Mechanics*, 788:R3, 2016. doi: 10.1017/jfm.2015.734.
- Sugan Durai Murugan and Samriddhi Sankar Ray. On the thermalization of the three-dimensional, incompressible, Galerkin-truncated Euler equation. *arXiv preprint arXiv:2209.05046*, 2022.
- J. Nocedal and S. J. Wright. *Numerical Optimization*. Springer, 1999.
- K. Ohkitani. A miscellany of basic issues on incompressible fluid equations. *Nonlinearity*, 21: 255–271, 2008.
- K. Ohkitani and P. Constantin. Numerical study of the Eulerian–Lagrangian analysis of the Navier-Stokes turbulence. *Phys. Fluids*, 20:1–11, 2008.
- P. Orlandi, S. Pirozzoli, and G. F. Carnevale. Vortex events in Euler and Navier-Stokes simulations with smooth initial conditions. *Journal of Fluid Mechanics*, 690:288–320, 2012.
- P. Orlandi, S. Pirozzoli, M. Bernardini, and G. F. Carnevale. A minimal flow unit for the study of turbulence with passive scalars. *Journal of Turbulence*, 15:731–751, 2014.
- R. B. Pelz. Symmetry and the hydrodynamic blow-up problem. *Journal of Fluid Mechanics*, 444:299–320, 2001.
- W. H. Press, B. P. Flannery, S. A. Teukolsky, and W. T. Vetterling. *Numerical Recipes*. Cambridge University Press, 1986.
- B. Protas. Systematic search for extreme and singular behaviour in some fundamental models of fluid mechanics. *Philosophical Transactions of the Royal Society A: Mathematical, Physical and Engineering Sciences*, 380(2225):20210035, 2022. doi: 10.1098/rsta.2021.0035. URL <https://royalsocietypublishing.org/doi/abs/10.1098/rsta.2021.0035>.
- A. Pumir and E. Siggia. Collapsing solutions to the 3D Euler equations. *Phys. Fluids A*, 2: 220–241, 1990.
- Cornelius Rampf, Uriel Frisch, and Oliver Hahn. Eye of the tyger: early-time resonances and singularities in the inviscid burgers equation. *arXiv preprint arXiv:2207.12416*, 2022.
- James C Robinson. The Navier-Stokes regularity problem. *Phil. Trans. R. Soc. A*, 378: 20190526, 2020. URL <http://doi.org/10.1098/rsta.2019.0526>.
- Hiroyuki Sato. Riemannian conjugate gradient methods: General framework and specific algorithms with convergence analyses, 2021.
- M. Siegel and R. E. Caflisch. Calculation of complex singular solutions to the 3D incompressible Euler equations. *Physica D*, 238:2368–2379, 2009.
- C. Sulem, P. L. Sulem, and H. Frisch. Tracing complex singularities with spectral methods. *Journal of Computational Physics*, 50:138–161, 1983.

- G. I. Taylor and A. E. Green. Mechanism of the production of small eddies from large ones. *Proceedings of the Royal Society of London A*, 158:499–521, 1937.
- Xi-Yuan Yin, Kai Schneider, and Jean-Christophe Nave. A Characteristic Mapping Method for the three-dimensional incompressible Euler equations. *arXiv preprint arXiv:2107.03504*, 2021.
- Dongfang Yun and Bartosz Protas. Maximum Rate of Growth of Enstrophy in Solutions of the Fractional Burgers Equation. *Journal of Nonlinear Science*, 28(1):395–422, Feb 2018. ISSN 1432-1467. doi: 10.1007/s00332-017-9412-3. URL <https://doi.org/10.1007/s00332-017-9412-3>.